Radboud Repository

Radboud University Nijmegen

PDF hosted at the Radboud Repository of the Radboud University Nijmegen

The following full text is a publisher's version.

For additional information about this publication click this link.
http://hdl.handle.net/2066/111196

Please be advised that this information was generated on 2017-12-06 and may be subject to change.

New Excitation Concepts for Ultra-High-Field Human MRI

Stephan Orzada

Erwin L. Hahn Institute for Magnetic Resonance Imaging

New Excitation Concepts for Ultra-High-Field Human MRI

Proefschrift

ter verkrijging van de graad van doctor

aan de Radboud Universiteit Nijmegen

op gezag van de rector magnificus prof. mr. S.C.J.J. Kortmann,

volgens besluit van het college van decanen

in het openbaar te verdedigen op dinsdag 28 mei 2013

om 10.30 uur precies

door

Stephan Orzada

geboren op 4 juli 1980

te Duisburg, Duitsland

Promotoren: Prof. dr. David G. Norris

Prof. dr. Mark E. Ladd, University Duisburg-Essen, Germany

Manuscriptcommissie: Prof. dr. Arend Heerschap
Prof. dr. Oliver Speck, Otto von Guericke University Magdeburg, Germany
Dr. Dennis Klomp, UMC Utrecht

The studies in this thesis were performed at the Erwin L. Hahn Institute for Magnetic Resonance Imaging in Essen, Germany.

ISBN: 978-3-00-041249-3

Copyright © 2012 by Stephan Orzada, all rights reserved.

The copyrights of the articles and illustrations that have been published or accepted for publication have been transferred to Medical Physics, American Institute of Physics, College Park, MD and Magnetic Resonance in Medicine, John Wiley & Sons Inc., Hoboken NY. The author has obtained the rights for their reproduction in this thesis.

Printed by: Universitätsdruckzentrum Duisburg-Essen, Duisburg, Germany

For my family.

Contents

List of original publications **9**

1 Introduction **10**

1.1 The historical background of magnetic resonance imaging 10

1.2 Principles of magnetic resonance imaging 12

1.3 Objective of this thesis 25

2 Open Design 8-Channel Transmit/Receive Coil for High-Resolution and Real-Time Ankle Imaging at 7 Tesla **31**

2.1 Introduction 32

2.2 Material and Methods 34

2.3 Results 39

2.4 Discussion 44

2.5 Conclusion 46

3 RF Excitation using Time Interleaved Acquisition of Modes (TIAMO) to Address B1 Inhomogeneity in Highfield MRI **50**

3.1 Introduction 51

3.2 Theory 53

3.3 Material and Methods 54

3.4 Results 61

3.5 Discussion 67

4 Time Interleaved Acquisition of Modes (TIAMO): an Analysis of SAR and Image Contrast Implications **71**

4.1 Introduction 72

4.2 Material and Methods 74

4.3 Results 79

4.4 Discussion 85

4.5 Conclusion 87

4.6 Appendix 88

5 Mitigation of B_1^+ Inhomogeneity on Single-Channel Transmit Systems with TIAMO **94**

5.1 Introduction 95

5.2 Material and Methods 97

5.3 Results 103

5.4 Discussion 106

5.5 Conclusion 108

6 Summary **112**

7 Samenvatting **114**

Acknowledgments **116**

Curriculum Vitae **118**

List of original publications

Portions of this thesis are published in the following international peer-reviewed journal articles with the author of this thesis as first author:

Orzada S, Bitz AK, Schäfer LC, Ladd SC, Ladd ME, Maderwald S.
"Open design eight-channel transmit/receive coil for high resolution and real-time ankle imaging at 7 T"
Med Phys., 2011; 38(3): 1150-1155

Orzada S, Maderwald S, Poser BA, Bitz AK, Quick HH, Ladd ME.
"RF excitation using time interleaved acquisition of modes (TIAMO) to address B1 inhomogeneity in high-field MRI"
Magn Reson Med., 2010;64(2):327-333

Orzada S, Maderwald S, Poser BA, Johst S, Kannengiesser S, Ladd ME, Bitz AK.
"Time-interleaved acquisition of modes: an analysis of SAR and image contrast implications"
Magn Reson Med., 2012;67(4):1033-1041.

Orzada S, Maderwald S, Johst S, Bitz AK, Solbach K, Ladd ME.
"Mitigation of B1+ inhomogeneity on single-channel transmit systems with TIAMO"
Magn Reson Med. 2012, [in press]

Additionally, another article has been published as first author which is not part of this thesis:

Orzada S, Maderwald S, Göricke SL, Parohl N, Ladd SC, Ladd ME, Quick HH
"Design and comparison of two eight-channel transmit/receive radiofrequency arrays for in vivo rodent imaging on a 7 T human whole-body MRI system"
Med Phys., 2010;37(5):2225-2232

Chapter 1 Introduction

1.1 The historical background of magnetic resonance imaging

When Wilhelm Conrad Röntgen discovered the x-ray phenomenon in November 1895 (1) it was quickly realized that the images that could be obtained were of great value to medical diagnostics. Since then more medical imaging techniques have emerged, of which magnetic resonance imaging is certainly one with the highest value in the diagnosis of soft tissue diseases.

The phenomenon of nuclear magnetic resonance was first described by Isidor Isaac Rabi in 1938 (2) in molecular beams. In 1944, he was awarded the Nobel Prize in Physics. In 1946, the technique was developed further by Felix Bloch (3) and Edward Mills Purcell (4), who independently expanded it for use in liquids and solids. Together, they shared the Nobel Prize in Physics in 1952.

The first person to demonstrate a potential use of NMR for medical purposes was Raymond Vahan Damadian. In 1971, he studied the differences in relaxation times between normal and cancerous tissue (5). He also filed the first patent for an MRI machine in 1972. However, this patent didn't include a description of a method for generating images.

The first to obtain 2D and later 3D MR images was Paul Lauterbur, who published this work in 1973 (6). He used linear gradients to achieve a frequency encoding in one dimension, providing him with multiple one-dimensional images similar to the techniques to obtain computer tomography (CT) images. Together with Peter Mansfield, who improved the image acquisition with what is known today as "echo planar imaging", he received the Nobel Prize in Physiology or Medicine in 2003.

Since the first clinical MR systems were installed in 1983, a constant drive to higher magnetic field strengths can be observed. This is due to the slightly more than linear increase of signal to noise (SNR) with field strength (7). While the first MR systems used magnetic fields of 0.35-0.5 Tesla, 1 Tesla and especially 1.5 Tesla

became the main workhorses in the clinical environment. 3 Tesla systems have now been introduced to the clinics and have gained market share over the last 10 years.

In 1997 an 8 Tesla magnet was installed at the Ohio State University and the first 7 Tesla system was installed as a research system at the University of Minnesota in 1999. Today, in 2012, 7 Tesla systems have not yet arrived in the clinical environment. One of the main problems in imaging any part of the human body at 7 Tesla are the inhomogeneities in the transmission field that appear due to the short wavelength of the radio frequency signals used to obtain excite the spin system (8). This problem is one of the main focuses in the research and development of ultra-high-field systems at 7 Tesla and above.

1.2 Principles of magnetic resonance imaging

Spins and magnetization

All elementary particles possess a quantum mechanical property called spin. For an easy understanding one can think of protons and neutrons as spheres that rotate around their axes. Atomic nuclei are composites of protons and neutrons. In a closed system, two spins always align anti-parallel, resulting in an overall spin of 0. Therefore, only nuclei with an odd number of protons and neutrons have a resulting spin and an angular momentum L.

Let an elementary particle be electrically charged or electrical charges within the sphere of a neutral elementary particle be unevenly distributed, then the current resulting from this rotation causes a magnetic field H that can be described by the magnetic moment μ

$$\vec{\mu} = \gamma \vec{L} \qquad [1.1]$$

Here γ is the gyromagnetic ratio which depends on the nucleus. Table 1.1 shows $\gamma/2\pi$ for some nuclei that are of importance in MRI. Since ^{1}H is the most common nucleus in human tissue, it has the greatest importance in MRI. Only nuclei with an uneven nucleon number have a resulting magnetic moment since the spins of the magnetic moments of two nucleons align anti-parallel to each other.

	^{1}H	^{13}C	^{19}F	^{23}Na	^{31}P
γ/2π (MHz/T)	42.58	10.71	40.08	11.27	17.25

Table 1.1: *γ/2π for different nuclei.*

In the absence of an external magnetic field, the magnetic moments within a sample of material point in randomly distributed directions, resulting in no effective moment. However, in the presence of a static magnetic field nuclei with spin 1/2 have two eigenstates corresponding to a precession of the magnetic moment around the axis of the direction of the magnetic field (z-direction) with

the z-component either oriented parallel or antiparallel. The frequency of this precession is called the Larmor frequency $\omega = \gamma B_0$. The probability for the parallel state is slightly higher, since the parallel state has a slightly lower energy level, and the ratio of parallel states to anti-parallel states can be described by the Boltzmann distribution:

$$\frac{N_-}{N_+} = e^{\frac{\gamma h B_0}{2\pi k T}} \qquad [1.2]$$

Here kT is the Boltzmann energy with k being the Boltzmann constant, $k = 1.38 \cdot 10^{-23} WsK^{-1}$, h is Planck's constant, $h = 6.626 \cdot 10^{-34} Js$, and B_0 is the absolute value of the external magnetic flux density $\vec{B}_0$. This means that there are more spins aligned parallel to $\vec{B}_0$ resulting in a very small, yet measurable, magnetic moment along the direction of $\vec{B}_0$ called the longitudinal equilibrium magnetization $\vec{M}_0$. For ^{1}H, considering the proton density ρ, this is given by

$$\vec{M}_0 = \frac{\rho \gamma^2 \pi^2 h^2 \vec{B}_0}{kT} \qquad [1.3]$$

Excitation and relaxation

The behavior of the resulting magnetic moment in the presence of an external radio frequency (RF) field, represented by the magnetic flux density $\vec{B}_1$ and in MRI often called the "B_1-field", is described by the Bloch equations:

$$\frac{dM_x(t)}{dt} = \gamma\left(\vec{M}(t) \times \vec{B}_1(t)\right)_x - \frac{M_x(t)}{T_2} \qquad [1.4]$$

$$\frac{dM_y(t)}{dt} = \gamma\left(\vec{M}(t) \times \vec{B}_1(t)\right)_y - \frac{M_y(t)}{T_2} \qquad [1.5]$$

$$\frac{dM_z(t)}{dt} = \gamma\left(\vec{M}(t) \times \vec{B}_1(t)\right)_z - \frac{M_z(t) - M_0}{T_1} \qquad [1.6]$$

Here T_1 and T_2 are time constants describing the process of restoring the equilibrium of the magnetic moment M_0 over time. The time constant T_1

describes the recovery of the longitudinal component M_z of the magnetization vector, while T_2 describes the decay of the transverse components M_x and M_y. The relaxation times T_1 and T_2 are tissue dependent.

From these equations one can deduce that a B_1 field rotating in the xy-plane at the Larmor frequency in the same direction that the magnetization vector is precessing around the z-axis can rotate the magnetization vector from the z-axis toward the xy-plane by an angle α, called the flip angle. For this reason the notation of the B_1-field is commonly split up into a portion that rotates clockwise along with the precession of the magnetic moment of the spin system (B_1^+) and a portion that rotates anti-clockwise (B_1^-):

$$B_1^+ = \frac{B_{1,x} + iB_{1,y}}{2} \qquad [1.7]$$

$$B_1^- = \frac{\left(B_{1,x} - iB_{1,y}\right)^*}{2} \qquad [1.8]$$

Here $B_{1,x}$ and $B_{1,y}$ denote the complex x and y components of the vector $\vec{B}_1$ of the local RF field. B_1^+ is referred to as the local transmit field, whereas B_1^- is referred to as the local receive field (9).

After the precessing magnetization vector is tipped away from the z-axis and the externally applied B_1-field is removed, the resultant magnetic flux can induce measurable voltage in a suitable conducting loop or other antenna. The received signal is the free induction decay (FID), which decays exponentially over time.

For a more in-depth description of spin dynamics and quantum mechanics, the reader is referred to standard textbooks (10,11).

Image formation

The application of a RF transmit field (clockwise polarized B_1-field) for a particular time is designated an excitation pulse. After an excitation pulse has

been transmitted, the whole area exposed to the excitation will generate a received FID as indicated above. This does not yield any information about the spatial composition of the materials in the sample. To gain such information, magnetic field gradients are used. These gradient fields change the value of the z-component of the magnetic field as a function of position. Commonly, linear gradients are used so that $B_z \propto \mathbf{r}$, where $\mathbf{r}$ is the position in the sample. These slight changes in magnetic field strength lead to a spatial dependency of the Larmor frequency that can be used to acquire information about the spatial composition of the materials. As an example, Figure 1.1 shows a simplified schematic of a 2D spin echo sequence, which will be explained in detail below.

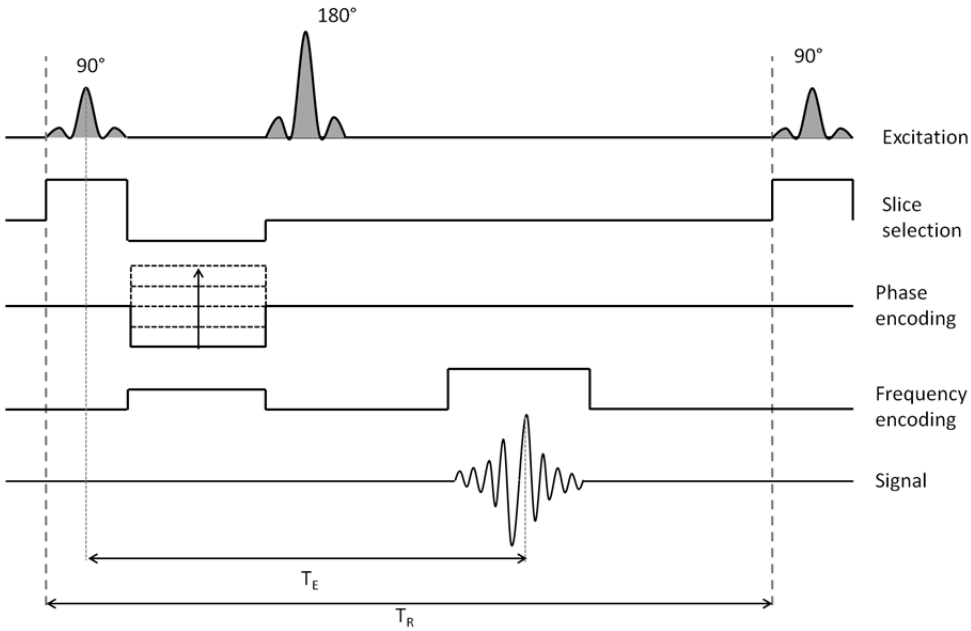

Figure 1.1: *Simplified schematic of a spin echo sequence. A 90° excitation pulse is played out while a slice selection gradient is applied. After this, a phase-encoding gradient is applied, followed by a 180° pulse to form a spin echo. During read out, a frequency-encoding gradient is applied.*

The sequence starts with a 90° excitation B_1 pulse. While this pulse is played out, a slice selection gradient is turned on along the z-direction, for example. This means that the Larmor frequency of the sample changes linearly in the z-direction. The width of the excited slice now depends on the steepness of the gradient as well as the bandwidth of the excitation pulse. Figure 1.2 illustrates this schematically.

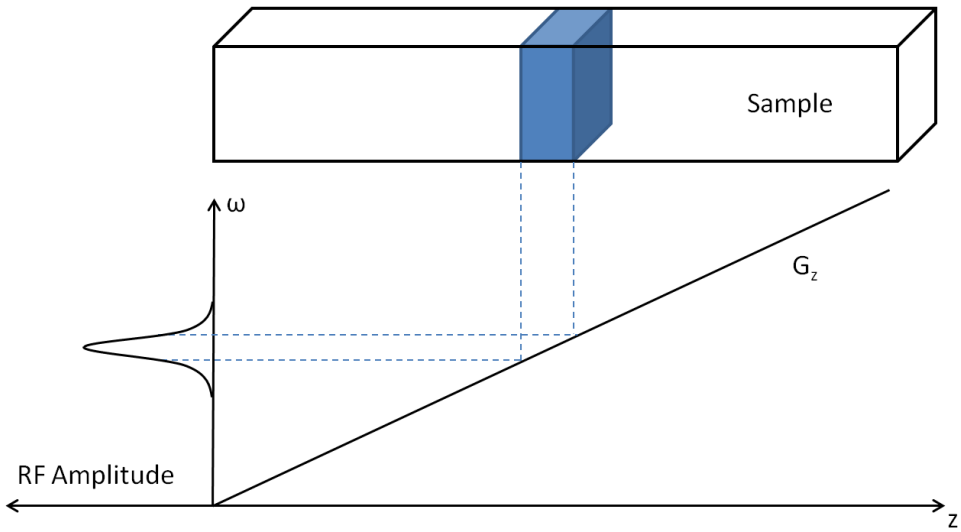

Figure 1.2: *Simplified depiction of slice selection. The thickness of the slice is dependent on the steepness of the gradient as well as on the bandwidth of the applied RF pulse.*

The slice-selection gradient is again applied after termination of the RF pulse with reversed direction to rephase the spins which were dephased during the excitation. A phase-encoding gradient is applied, for example in the y-direction, to create a spatial dependence of the spin phases within the sample. After this, a 180° B_1 pulse is played out. In this way, any dephasing due to local magnetic field inhomogeneities and susceptibility effects (T_2* decay) is revoked, and spins that have dephased due to this effect rephase again. During readout, a frequency-encoding gradient is applied, for example in the x-direction. This gradient causes

the spins to precess at different frequencies. A spectral analysis of the received signal then provides spatial information along the x-direction.

The time between the 90° excitation pulse and the maximum of the received signal is twice the time between the 90° pulse and the 180° pulse and is called the echo time T_E. After reception of the signal, the same procedure is repeated with a phase-encoding gradient of a different strength. The time between these repetitions is called the repetition time T_R. In this way, the Fourier transformation of the image, called the k-space, is filled line by line. The image can be calculated by inversely Fourier transforming the k-space.

For more information about pulse sequences, the reader is referred to the Handbook of MRI Pulse Sequences (12).

Parallel imaging

Image acquisition in MRI is time consuming due to the line by line acquisition and repetition times in the order of approximately 5 ms to 3000 ms.

To speed up the acquisition, parallel imaging techniques have been developed which allow acquisition of undersampled data sets in the phase-encoding direction. The reduction factor R denotes the speed-up that is achieved by only acquiring every Rth line in k-space. To be able to do so without foldover artifacts due to not satisfying the Nyquist criterion, these parallel imaging techniques exploit the spatial information of the different reception (B_1^-) profiles of the individual elements of a receive array.

The most notable of these parallel imaging techniques are the image-based SENSE (13) technique and the k-space-based GRAPPA (14) technique. Both have in common that they need information about the receive profiles of the elements of the receive array. In SENSE this is normally acquired separately, while in GRAPPA this information is usually obtained directly as part of the pulse sequence by acquiring extra lines near the center of k-space.

Since only a factor of 1/R samples are acquired, the SNR of an accelerated image is reduced by $1/\sqrt{R}$. Furthermore, the SNR is reduced by the array specific g-factor g(R,**r**), which is a function of the reduction factor and is spatially dependent. Thus, in accelerated images the SNR is not homogeneously distributed. For GRAPPA the g-factor distribution is usually much smoother than for SENSE. The g-factor is an important value in the characterization of receive arrays, as it is a good indicator of how high the practical acceleration can be using the array. An efficient way to calculate the g-factor is the pseudo multiple replica technique (15) in which an image is reconstructed many times with added artificial noise. In this way, the acquisition of many images can be simulated. Afterwards, the mean and standard deviation of each pixel across the set of images is calculated to determine the SNR for different acceleration factors. By comparing the SNR to the SNR of the unaccelerated case, the g-factor can be calculated.

Figure 1.3 shows an example of the g-factor of an 8-channel transmit/receive head array combined with a 7-channel receive array (16) in a spherical phantom filled with tissue simulating liquid. It is clearly discernable that the g-factor is much lower in the vincinity of the additional array, where the increased number of elements with distinct sensitivities leads to an increase in acceleration capability.

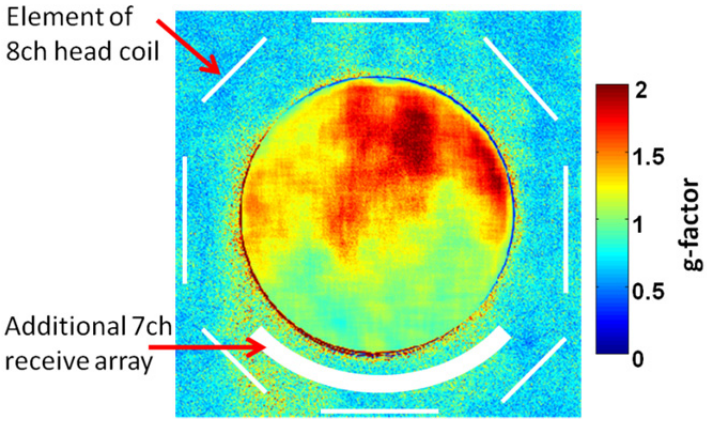

Figure 1.3: *Measured g-factor for a combination of an 8-channel transmit/receive head array and an additional 7-channel receive array loaded with a sphere of 15 cm diameter filled with tissue simulating liquid. The reduction factor is R = 4. The phase-encoding direction is from left to right.*

Parallel transmit

Since the resonance frequency is proportional to the strength of the main magnetic field, the constant drive to higher field strengths to gain SNR also results in a decreasing wave length of the RF signals used for excitation. At 1.5 T the resonance frequency is approximately 64 MHz. The resulting wave length in free space is therefore about 4.6 m. The wavelength of an electromagnetic wave is proportional to the inverse of the square root of the dielectric permittivity of the medium it travels through. On average the human body has a dielectric permittivity of $\varepsilon_{r,body,1.5T} \approx 80$ at 1.5 T, so inside the tissue the wavelength is about 50 cm, which is still much larger than the diameter of a human body. Looking at 7 T with a resonance frequency of ca. 300 MHz and $\varepsilon_{r,body,7T} \approx 40$, the wavelength inside the tissue is reduced to about 15 cm, which is approximately the diameter of a human head. The phase of the RF field inside the tissue can no longer be assumed uniform as at 1.5 T, and phase effects can lead to strong inhomogeneity

caused by destructive interferences when imaging the human body at 7 Tesla and above (8,17-19). This has a strong influence on the quality of the image.

For a gradient echo image with a long repetition time, the signal $S(\mathbf{r})$ at a location r is proportional to

$$S_{GE}(\mathbf{r}) \propto |\sin(\gamma B_1^+(\mathbf{r})T)| \qquad [1.9]$$

assuming a rectangular excitation pulse of length T. For spin echo imaging, the relation to the transmit field is of even higher order and can be approximated as

$$S_{SE}(\mathbf{r}) \propto |\sin^3(\gamma B_1^+(\mathbf{r})T)| \qquad [1.10]$$

Spatial variations in the excitation field B_1^+ not only have an influence on the signal to noise distribution, but also on the contrast distribution. Due to varying flip angles across an image, the contrast between different tissues may vary, making diagnosis difficult or even impossible. An example of inhomogeneous excitation can be seen in Figure 1.4.

To overcome this inhomogeneity problem, many techniques have been proposed. The two most widely considered are RF shimming (20,21) and Transmit SENSE (22-24), and shall be briefly introduced in the following.

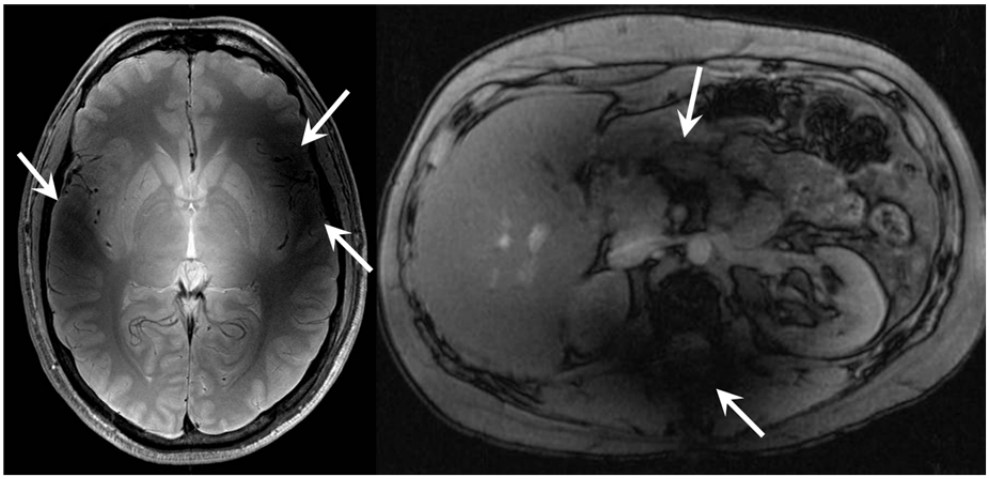

Figure 1.4: *Two MR images with visible signal dropouts due to inhomogeneous excitation (arrows) acquired at 7 Tesla. On the left an axial spin echo image of a human head is shown, on the right an axial gradient echo image of the human abdomen.*

RF shimming

In RF shimming, the principle of superposition is used. Similar to phased arrays in radar technology ("beam forming"), for example, an array of multiple elements is used to transmit a signal. Each element transmits the same pulse profile but with constant amplitude and phase settings which vary between elements. Thus, the resulting field $B^{+}_{1,total}$ is the complex sum of all the fields of the *N* individual elements weighted with a complex amplitude *a*:

$$B(\mathbf{r})^{+}_{1,total} = \sum_{n=1}^{N} a \cdot B(\mathbf{r})^{+}_{1,n} \qquad [1.11]$$

This expression can easily be formulated into a system of complex equations and solved for a desired resulting $B^{+}_{1,total}$ using an appropriate optimization routine. Since there is one equation for all spatial sampling points, the system of equations is typically overdetermined. Typical target distributions are a

homogeneous distribution within a region of interest, which can cover the complete field of view (uniformity shim), or a maximization of $B_{1,total}^{+}$ in a certain area (efficiency shim).

Figure 1.5 shows an example of RF shimming in the abdomen of a healthy volunteer using a flexible 8-channel transmit array (22). The left image was acquired with a circularly polarized mode (45° phase increment between the neighboring elements, which were distributed circumferentially around the liver). A significant signal dropout in the posterolateral portion of the liver (arrow) is visible. The right image shows the same slice acquired with a shim optimized for homogeneity in the right body region. The signal dropout is significantly reduced, increasing the diagnostic value of the image in the area of the liver.

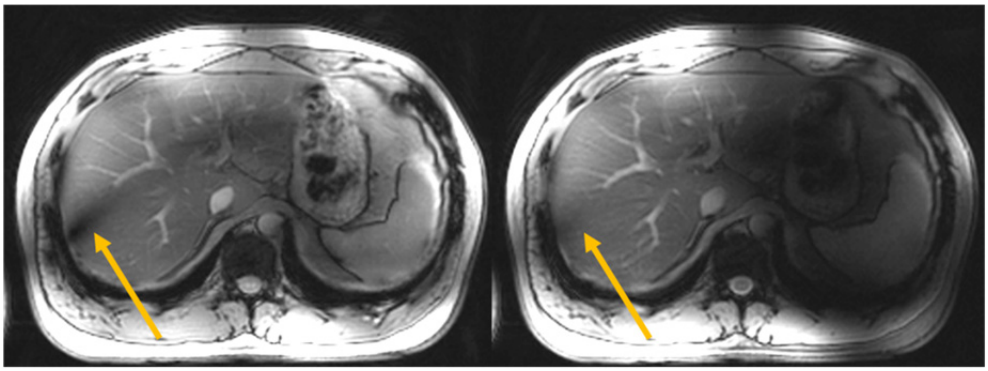

Figure 1.5: *Abdominal T1-weighted FLASH images from a human volunteer. The left image was acquired with a phase increment of 45° between neighboring elements. The right image was acquired with a shim optimized for homogeneity in the right body region. The signal dropout (arrows) is significantly reduced by the dedicated RF shim.*

Transmit SENSE

Transmit SENSE (23-25) is a technique for spatial selective excitation with a multitude of parallel transmit channels. Like RF shimming it utilizes different

transmission profiles $B(\mathbf{r})_{1,n}^{+}$ on the different transmit elements. In contrast to RF shimming, the complex weighting of each channel is not static, but can vary with time. In addition, the gradients of the MR system are used to provide spatial encoding during transmission. In this way it is possible to produce virtually any kind of excitation profile within a region of interest. In the following, this shall briefly be explained using the image domain based technique proposed by Grissom (26).

The starting point is the small tip angle approximation (27). Neglecting eventual inhomogeneities of the main magnetic field $\Delta B_0(\mathbf{r})$, this can be written as:

$$M_{xy}(\mathbf{r}) = iM_0\gamma s^{+}(\mathbf{r}) \int_0^T b(t)e^{i\mathbf{r}\mathbf{k}(t)}\mathrm{d}t \qquad [1.12]$$

Here $s^{+}(\mathbf{r}) = \frac{B(\mathbf{r})_1^{+}}{I}$ is the normalized transmit sensitivity of the transmitting element and $b(t)$ is a normalized modulation function describing the excitation waveform used. The integral describes a Fourier transform from the time domain to the space domain, where

$$\mathbf{k}(t) = -\gamma \int_t^T \mathbf{G}(s)\mathrm{d}s \qquad [1.13]$$

is the k-space trajectory which relates the position in k-space to the time signal. Here **G** describes the time varying gradient fields, while T is the total time of the excitation.

For a number of coils N_c which are used in parallel, the small tip angle approximation can be expanded using the principle of superposition.

$$M_{xy}(\mathbf{r}) = iM_0\gamma \sum_{l=1}^{N_c} s_l^{+}(\mathbf{r}) \int_0^T b_l(t)e^{i\mathbf{r}\mathbf{k}(t)}\mathrm{d}t \qquad [1.14]$$

If the time is discretized to a number of samples N_t and space is discretized to N_s samples, this can be formed into a set of $N_{equ} = N_c \cdot N_t$ linear equations. It is not necessary that $N_t = N_s$. By choosing $N_t < N_s$ it is possible to exploit the different transmission profiles of the transmit elements to speed up the excitation while

maintaining the desired excitation profile. As an example, the left image of Figure 1.5 shows the logo of the Erwin L. Hahn Institute for MRI, while the right image of the same figure shows the pattern of the logo excited inside a spherical oil phantom using an 8-channel transmit/receive head array (28).

Figure 1.6: *On the left the logo of the Erwin L. Hahn Institute for MRI is shown, on the right the pattern of the logo as excited in a spherical oil phantom using an 8-channel transmit/receive head array.*

Transmit SENSE requires complicated and therefore expensive hardware, since each element needs its own RF transmission chain. The transmission by the multiple elements must be sychronised to a high degree both with each other, and with the simultaneously applied gradient waveforms. Furthermore, one needs very accurate knowledge of the B_1^+ distribution of each transmit element.

1.3 Objective of this thesis

The aim of this thesis is to develop new techniques for 7 Tesla imaging of the human body, with a strong focus on imaging outside of the brain. To reach this goal, new RF coils and equipment had to be developed to be able to make use of the newly developed imaging scheme Time Interleaved Acquisition of Modes (TIAMO) presented in this thesis.

First, in chapter 2 an 8-channel U-shaped micro strip array for in vivo imaging of the human ankle is presented as an example of arrays that had to be developed in order to perform the imaging experiments in the further chapters (22,28-29). The ankle array's U-shaped form facilitates free posturing and movement of the ankle to enable real-time imaging of ankle movement as well as high resolution imaging. The prototype is characterized in numerical experiments and bench measurements, and first in vivo images are shown.

To facilitate large field of view imaging at 7 Tesla without the signal dropouts described in the introduction, a new technique called TIAMO is presented in chapter 3. In contrast to techniques like RF shimming and Transmit SENSE, TIAMO does not aim to achieve a homogeneous excitation, rather a homogeneous SNR distribution as well as a homogeneous contrast. The same image is acquired twice (or more) in a line by line interleaved fashion with two (or more) different RF shims which have signal dropouts in different locations. The root sum of squares of the two images will not show these signal dropouts. The increased acquisition time for acquiring multiple images is reduced by using "virtual elements" formed from the datasets and a GRAPPA reconstruction. The theory as well as first experiments regarding SNR and g-factor are presented.

Since the indiviudal images in TIAMO are acquired with inhomogneoeus excitation, a closer look at the impact on image contrast is necessary. Furthermore, SAR is a key factor in MRI, and an investigation of the impact of TIAMO on SAR is important get a measure of its usefulness. This is done in chapter 4, where the theory of image contrast in TIAMO for spoiled gradient echo images is derived and MRI experiments are performed to show that imaging with TIAMO

is feasible for a multitude of contrasts. Also, extensive numerical experiments are presented showing the impact of TIAMO on image homogeneity and SAR in three different body models with two different RF coils each.

TIAMO, as well as most techniques used to acquire homogeneous images of the body at 7 Tesla, is a multichannel transmit technique. Multichannel transmit requires sophisticated hardware for the generation of the transmit signals as well as for supervision of patient safety. In chapter 5 a very inexpensive hardware setup is presented that makes it possible to use TIAMO on standard single-channel transmit systems with only single-channel SAR supervision. The setup consists of a high-power RF switch, a control unit developed for operation with TIAMO, and a Butler matrix. The setup is tested regarding safety in bench measurements, and first in vivo images of the human pelvis show that spin echo imaging at 7 Tesla is feasible with a single-channel setup and TIAMO.

The work in chapters 2 to 5 has already been published, and these chapters are formatted accordingly. TIAMO has been used in a variety of experiments such as abdominal imaging (29-31), breast imaging (32), and even whole-body imaging from head to toe (28). Currently, TIAMO is starting to be used in clinical studies to increase the homogeneity in 7 Tesla body imaging, for example for non-enhanced MRA of the lower extremities (33,34), because of its robustness and very short preparation time.

Chapter 6, the last chapter, provides a brief summary and discussion.

References

1. Knutson F. Röntgen and the Nobel Prize. The discussion at the Royal Swedish Academy of Sciences in Stockholm 1901. Acta Radiol Diagn 1974;15((5)):465-473.

2. Rabi I, Zacharias J, Millman, Kusch P. A new method of measuring nuclear magnetic moment. Physical Review 1938;53((4)):318.

3. Bloch F, Hanson W, Packard M. Nuclear induction. Phys Rev 1946;69:127.

4. Purcell E, Torrey H, Pound R. Resonance absorption by nuclear magnetic moments in a solid. Phys Rev 1946;69:37-38.

5. Damadian RV. Tumor Detection by nuclear magnetic resonance. Science 1971;171:1151-1153.

6. Lauterbur P. Image Formation by Induced Local Interactions: Examples of employing nuclear magnetic resonance. Nature 1973;242((5394)):190-191.

7. Hoult DI, Phil D. Sensitivity and power deposition in a high-field imaging experiment. J Magn Reson Imaging 2000;12(1):46-67.

8. Van de Moortele PF, Akgun C, Adriany G, Moeller S, Ritter J, Collins CM, Smith MB, Vaughan JT, Ugurbil K. B(1) destructive interferences and spatial phase patterns at 7 T with a head transceiver array coil. Magn Reson Med 2005;54(6):1503-1518.

9. Hoult DI. The principle of reciprocity in signal strength calculations - A mathematical guide. Concepts Magn Reson 2000;12:173-187.

10. Haacke E, Brown R, Thompson M, Venkatesan R. Magnetic Resonance Imaging, physical principles and sequence design: John Wiley & Sons, Inc.; 1999.

11. Levitt M. Spin dynamics, basics of nuclear magnetic resonance: John Wiley & Sons, Ltd.; 2001.

12. Bernstein M, King K, Zhou X. Handbook of MRI Pulse Sequences: Elsevier Academic Press; 2004.

13. Pruessmann KP, Weiger M, Scheidegger MB, Boesiger P. SENSE: sensitivity encoding for fast MRI. Magn Reson Med 1999;42(5):952-962.

14. Griswold MA, Jakob PM, Heidemann RM, Nittka M, Jellus V, Wang J, Kiefer B, Haase A. Generalized autocalibrating partially parallel acquisitions (GRAPPA). Magn Reson Med 2002;47(6):1202-1210.

15. Robson PM, Grant AK, Madhuranthakam AJ, Lattanzi R, Sodickson DK, McKenzie CA. Comprehensive quantification of signal-to-noise ratio and g-factor for image-based and k-space-based parallel imaging reconstructions. Magn Reson Med 2008;60(4):895-907.

16. Orzada S, Kraff O, Rabe K, Timman-Braun D, Ladd ME. A 7-channel receive array insert for enhancement of SNR and acquisition speed in the cerebellum and visual cortex at 7T. In: Proceedings of the 18th Annual Meeting of ISMRM, Stockholm, Sweden 2010;(Abstract 3850).

17. Snyder CJ, Delabarre L, Metzger GJ, van de Moortele PF, Akgun C, Ugurbil K, Vaughan JT. Initial results of cardiac imaging at 7 tesla. Magn Reson Med 2008.

18. Vaughan JT, Snyder CJ, DelaBarre LJ, Bolan PJ, Tian J, Bolinger L, Adriany G, Andersen P, Strupp J, Ugurbil K. Whole-body imaging at 7T: preliminary results. Magn Reson Med 2009;61(1):244-248.

19. Umutlu L, Orzada S, Kinner S, Maderwald S, Brote I, Bitz AK, Kraff O, Ladd SC, Antoch G, Ladd ME, Quick HH, Lauenstein TC. Renal imaging at 7 Tesla: preliminary results. European radiology;21(4):841-849.

20. Collins CM, Liu W, Swift BJ, Smith MB. Combination of optimized transmit arrays and some receive array reconstruction methods can yield homogeneous images at very high frequencies. Magn Reson Med 2005;54(6):1327-1332.

21. Mao W, Smith MB, Collins CM. Exploring the limits of RF shimming for high-field MRI of the human head. Magn Reson Med 2006;56(4):918-922.

22. Orzada S, Quick HH, Ladd ME, Bahr A, Bolz T, Yazdanbakhsh P, Solbach K, Bitz AK. A flexible 8-channel transmit/receive body coil for 7 T human imaging. In: Proceedings of the 17th Annual Meeting of ISMRM, Honolulu, HI, USA 2009; (Abstract 2999).

23. Katscher U, Bornert P, Leussler C, van den Brink JS. Transmit SENSE. Magn Reson Med 2003;49(1):144-150.

24. Katscher U, Bornert P, van den Brink JS. Theoretical and numerical aspects of transmit SENSE. IEEE transactions on medical imaging 2004;23(4):520-525.

25. Katscher U, Rohrs J, Bornert P. Basic considerations on the impact of the coil array on the performance of Transmit SENSE. Magma (New York, NY 2005;18(2):81-88.

26. Grissom W, Yip CY, Zhang Z, Stenger VA, Fessler JA, Noll DC. Spatial domain method for the design of RF pulses in multicoil parallel excitation. Magn Reson Med 2006;56(3):620-629.

27. Pauly J, Nishimura D, Macovski A. A k-space analysis of small-tip-angle excitation. J Magn Reson 1989;81:43-56.

28. Orzada S, Kraff O, Schäfer LC, Brote I, Bahr A, Bolz T, Maderwald S, Ladd ME, Bitz AK. 8-channel transmit/receive head coil for 7 T human imaging using intrinsically decoupled strip line elements with meanders. In:

Proceedings of the 17th Annual Meeting of ISMRM, Honolulu, HI, USA 2009; (Abstract 3010).

29. Orzada S, Maderwald S, Kraff O, Brote I, Ladd ME, Solbach K, Yazdanbakhsh P, Bahr A, Fautz H-P, Bitz AK. 16-channel Tx/Rx body coil for RF shimming with selected Cp modes at 7T. In: Proceedings of the 18th Annual Meeting of ISMRM, Stockholm, Sweden 2010;(Abstract 50).

30. Orzada S, Johst S, Bitz AK, Kraff O, Brote I, Ladd SC, Ladd ME, Maderwald S. 7 Tesla Abdominal Imaging using TIAMO. In: Proceedings of the 19th Annual Meeting of ISMRM, Montreal, Canada 2011;Abstract 594.

31. Orzada S, Maderwald S, Oehmigen M, Ladd ME, Solbach K, Bitz AK. An 8-channel TX, 16-channel RX flexible body coil at 7 Tesla using both branches of centrally fed strip lines as individual receive elements. In: Proceedings of the 18th Annual Meeting of ISMRM, Stockholm, Sweden 2010;(Abstract 641).

32. Orzada S, Maderwald S, Kopp L, Ladd ME, Nassenstein K, Bitz AK. A 16-Channel Micro Strip Tx/Rx Array for Bilateral Breast Imaging at 7 Tesla. In: Proceedings of the 20th Annual Meeting of ISMRM, Melbourne, Australia 2012;(Abstract 901).

33. Fischer A, Maderwald S, Orzada S, Johst S, Ladd ME, Nassenstein K, Umutlu L, Lauenstein TC. Native MR-Bildgebung der Becken-Bein-Gefäße bei 7 Tesla: erste Ergebnisse. In: Proceedings of 93 Deutscher Röntgenkongress, Hamburg, Germany 2012.

34. Fischer A, Maderwald S, Orzada S, Johst S, Schäfer LC, Ladd ME, Nassenstein K, Umutlu L, Lauenstein TC. Non-enhanced MRA of the lower extremity vessels at 7 Tesla: initial experience. Investigative Radiology (Submitted) 2012.

Chapter 2 Open Design 8-Channel Transmit/Receive Coil for High-Resolution and Real-Time Ankle Imaging at 7 Tesla*

Abstract

At 1.5 T real-time MRI of joint movement has been shown to be feasible. 7 T, however, provides higher SNR and thus an improved potential for parallel imaging acceleration. The purpose of this work was to build an open, U-shaped 8-channel transmit/receive microstrip coil for 7 tesla MRI to enable high resolution and real-time imaging of the moving ankle joint.

A U-shaped 8 channel transmit/receive array for the human ankle was built. S-parameters and g-factor were measured. SAR calculations of different ankle postures were performed to ensure patient safety. Inhomogeneities in the transmit field consequent to the open design were compensated for by the use of static RF shimming. High resolution and real-time imaging was performed in human volunteers.

The presented array showed good performance with regard to patient comfort and image quality. High acceleration factors of up to 4 are feasible without visible acceleration artifacts. Reasonable image homogeneity was achieved with RF-shimming.

Open, non-cylindrical designs for transmit/receive coils are practical at 7 T and real time imaging of the moving joint is feasible with the presented coil design.

*__Orzada S__, Bitz AK, Schäfer LC, Ladd SC, Ladd ME, Maderwald S.
"Open design eight-channel transmit/receive coil for high resolution and real-time ankle imaging at 7 T"
Med Phys., 2011; 38(3): 1150-1155

2.1 Introduction

With the availability of human MR systems above 3 tesla with multichannel receive and multichannel transmit systems, many new prospects have been opened for the imaging community. Parallel imaging techniques such as SENSE [1] and GRAPPA [2] already allow for acceleration of image acquisition at clinically used field strengths. Higher field strengths inherently lead to better performance of these parallel imaging techniques [3,4] by means of an increased signal-to-noise ratio (SNR) and an increased distinctness in the sensitivity patterns of individual coil elements. Furthermore, when parallel transmission techniques such as transmit SENSE [5,6] or RF shimming [7,8] are available, non-cylindrical transmit arrays can potentially be used for excitation, theoretically enabling moving joint imaging with an open array shaped for this purpose. Transmit and receive transmission line arrays [9] have been shown to achieve good performance in 7 T non-cylindrical arrays [10].

Real-time MRI of joint movement has been shown to be feasible at 1.5 T [11]. 7 T, however, provides higher SNR and thus an improved potential for parallel imaging acceleration [12]. The higher SNR is an optimal prerequisite for real-time imaging, i.e. for moving joint MRI. In addition, cartilage imaging at 7 T highly profits from new and enhanced contrasts [13]. Imaging the function or changes in morphology or hydration of cartilage and ligaments during movement at 7 T, however, has been so far impossible due to lack of suitable coils. Due to the lack of a body coil at 7 T, all arrays must have the capability for both transmission and reception, so the demands on the design are distinctly different from those for 1.5 T receive-only arrays.

The purpose of this work was thus to build an open, U-shaped 8-channel transmit/receive microstrip coil for 7 T MRI. This open coil design offers sufficiently free movement to allow motion of the ankle joint during measurement of the subject's foot. Inhomogeneities in the transmit field consequent to the open design are compensated for by the use of static RF shimming. High spatial and temporal resolution static imaging as well as real-time

joint imaging of the human ankle in vivo is performed. Coil characterizations including S-parameters and g-maps are provided as well.

2.2 Materials and Methods

Coil design

The array consists of 8 microstrip modules arranged in a U-shape (Figure 2.1A). Each module has a width of 5 cm and a length of 22.5 cm. The strips are 15 cm long and 0.75 cm wide, the distance from the strip to the ground plane is 0.9 cm. The modules are built as inverted microstrip lines [14]. The two posterior modules are tilted by 30° out of the horizontal plane, the adjacent modules are tilted by 70°, and the four remaining modules are arranged vertically.

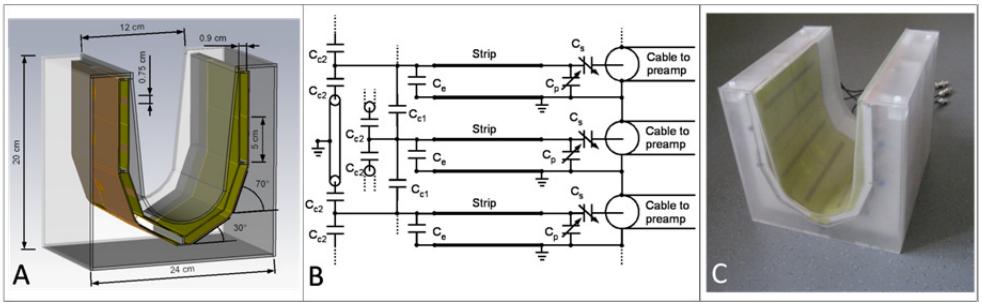

Figure 2.1: *A) Mechanical drawing; B) electrical schematic showing 3 out of 8 microstrip lines, including the decoupling network on the left of the schematic; C) photograph of the open U-shaped ankle coil.*

Figure 2.1B shows the electrical schematic of the array. The distal end of each strip is connected to the ground plane with an end capacitor C_e = 6.8 pF to create a standing wave on the microstrip line with the current maximum in the center of the line, since the current distribution on a lossless transmission line is solely dependent on the termination. The matching network consists of a tunable series capacitor C_s = 0.7-2.0 pF and a tunable parallel capacitor C_p = 2.5-12.0 pF to match the microstrip line to the 50 Ohm feeding line. To optimize decoupling, the end of each strip is connected to the nearest and next nearest neighbors. The connection to the nearest neighboring element is realized with a coupling capacitor C_{c1} = 0.7 pF. The connection to the next nearest neighbors is accomplished with a second coupling capacitor C_{c2} = 1.0 pF interconnected with 100 mm of semi-rigid

coaxial cable necessary to bridge the distance. There is no mechanical or electrical connection over the opening of the U-shaped array. The ground planes of all modules are interconnected with capacitors C_g = 1000 pF to reduce eddy currents (not shown in Figure 2.1). Three of these capacitors are placed on both sides of each module, at the ends of the modules as well as in the center. Cable traps made from loops of semi rigid cable with a parallel capacitor are included in the cables to the preamps to prevent shield currents, and the preamps (50 Ω, Stark Contrast, Erlangen, Germany) are located in a multipurpose preamplifier box with T/R-switches (Stark Contrast, Erlangen, Germany) about 30 cm away from the coil.

The housing (Figure 2.1C) for the coil is made from semi-transparent Plexiglas (PMMA) with a thickness of 3 mm. Its height, width, and length are 20 cm, 21.5 cm and 24 cm, respectively. The U-shaped opening is 12 cm wide at the top and is slightly tapered toward the bottom.

All circuit boards used in the 8-channel U-shaped ankle array were produced with a Protomat H60 milling machine (LPKF Laser & Electronics AG, Garbsen, Germany) from 1.5 mm thick FR4 circuit board with 35 µm copper foil. All fixed-value capacitors were non-magnetic capacitors with a DC working voltage of up to 1000 V (11 Series, Voltronics Corporation, Denville, NJ, USA); the trimmer capacitors were TZ03_F series capacitors (muRata Manufacturing Co. Ltd., Kyoto, Japan).

Workbench measurements

S-parameter measurements were performed with a network analyzer E5061A (Agilent Technologies, Santa Clara, CA, USA) while the coil was loaded with a human subject.

SAR calculations

SAR (specific absorption rate) calculations were performed using CST Microwave Studio (CST AG, Darmstadt, Germany) and the male model (DUKE) from the Virtual Family [15] with 2 mm resolution and 80 unique tissue types. The complete matching and decoupling networks were simulated in a SPICE-based co-simulation. The simulations were performed for three different ankle postures to find the worst-case SAR during patient movement: the original posture of the ankle of the DUKE model was flexed by 25 degrees about the ankle joint in both directions.

MR imager

All images were acquired on a Siemens 7T whole-body system (Magnetom 7T, Siemens Healthcare, Erlangen, Germany) using gradients with maximum amplitude of 40 mT/m and maximum slew rate of 200 mT/m/ms. This system is equipped with a custom-built 8-channel RF shimming system [16]. A pre-calculated (simulation-based) B_1 shim to optimize transmit homogeneity was applied to the system; SAR calculations were performed beforehand based on this shim.

Phantom measurements

For phantom measurements, a cylindrical phantom with a diameter of 7.8 cm and a length of 15 cm filled with tissue-simulating liquid (mass fraction: 37.5 % water, 56.5 % sugar, 6 % salt; $\varepsilon_r = 46.3$, $\sigma = 0.8\ \Omega^{-1}\ m^{-1}$) was used. The electrical parameters are close to the mean electrical parameters of the Duke model ($\varepsilon_r = 41.6$, $\sigma = 0.6\ \Omega^{-1}\ m^{-1}$). The phantom was placed on the same 2.5 cm thick foam cushion which is used for human subjects. To provide a measure of the homogeneity of the array's SNR distribution, SNR in this homogeneous phantom was measured using an axial and saggital gradient-echo sequence with 160 by 160 mm FOV and a dual acquisition and subtraction method [17].

B_1 mapping

B_1 mapping was performed in vivo using the actual flip angle method [18] with an isotropic 4.6 mm resolution. The pulse length was 250 µs and the system's transmit amplitude was chosen to be 150 V.

GRAPPA g-factor estimation

To estimate the GRAPPA g-factor of the array and thus the acceleration capability, a pseudo multi replica method [19] was used. A fully sampled axial gradient echo image of a volunteers ankle was acquired with an image matrix of 384 by 384. For the pseudo multi replica approach openGRAPPA [2] was used (reconstruction parameters: 48 autocalibration lines for reduction factors of R = 2, 3, and 4). The phase-encoding direction was anterior-posterior.

In vivo imaging

In vivo imaging was performed with 3 healthy volunteers with approval of the local ethics committee.

To improve subject comfort and ensure stable positioning, a soft foam cushion with a thickness of 2.5 cm was placed around the ankle. The cushion stabilizes the ankle but is cut away around the forefoot, so that free movement of the forefoot in the head-feet direction is possible.

For static structural imaging, three different sequences were used: a PD/T2-weighted 2D Turbo Spin-Echo (TSE) sequence with an echo train length of ETL = 5, a 3D Dual Echo Steady State (DESS), and an isotropic T1-weighted 3D spoiled gradient-echo (FLASH) sequence.

For real-time imaging, two types of sequences were used: a steady-state precession gradient-echo sequence (TrueFISP) similar to the proposed method in

Quick, et al. [11] but without echo sharing as well as a TurboFLASH sequence. Single sagittal sections were used with phase encoding in the anterior-posterior direction. To achieve a high temporal resolution, GRAPPA acceleration with a nominal reduction factor R of 4 was used in both sequences. Thus, the TrueFISP images could be acquired with a temporal resolution of 2.5 images per second and the TurboFlash with 3 images per second. Both sequences were repeated until an overall measurement time of approximately 30 seconds was reached.

Table 2.1 presents the relevant sequence parameters for both static and real-time imaging.

Sequence	Resolution [mm^3] (non-interpolated)	TR [ms]	TE [ms]	BW [Hz/pixel]	FA [°]	Matrix	R_{nom}	$N_{reflines}$	TA [min:s]
TSE	0.35 x 0.35 x 2	4190	34 / 91	325	90	512 x 480 x 10	2	48	6:39
3D DESS	0.35 x 0.35 x 1.5	10.61	4.1	390	15	512 x 512 x 128	2	48	4:13
3D FLASH	0.42 x 0.42 x 0.42	6.62	3.06	340	7.5	320 x 290 x 160	2	48	2:55
TrueFISP	0.81 x 0.81 x 4.0	407	2.75	560	70	224 x 224 x 1	4	24	0:00.4
TurboFLASH	1.16 x 1.16 x 4.0	339	1.52	465	8	256 x 256 x 1	4	48	0:00.3

Table 2.1: *Imaging parameters for static and real-time imaging in human volunteers*

2.3 Results

Workbench measurements

The reflection coefficient and the coupling were found to be dependent on the posture of the ankle of human subjects in the coil lab; however, the reflection factor S_{11} always remained below -13 dB when varying the posture of the ankle inside the coil. The coupling to neighboring elements S_{21} was below -14 dB and the coupling to next neighbors S_{31} was below -20 dB.

SAR calculations

Figure 2.2 shows the 10g-averaged SAR distributions for the three simulated ankle postures. The relative phases of the shim setting were 121°, 201°, 311°, 322°, 0°, 96°, 151° and 278° in the clockwise direction. All relative amplitudes were the same. The maximum allowed input power for the three cases were 4.2 W, 8.8 W and 7.7 W. Local SAR varies by a factor of 2.1 through the different ankle postures. The maximum SAR occurs in the heel in Figure 2.2A. To provide a safety margin, the maximum permitted continuous input power for in vivo imaging was set to 4 W.

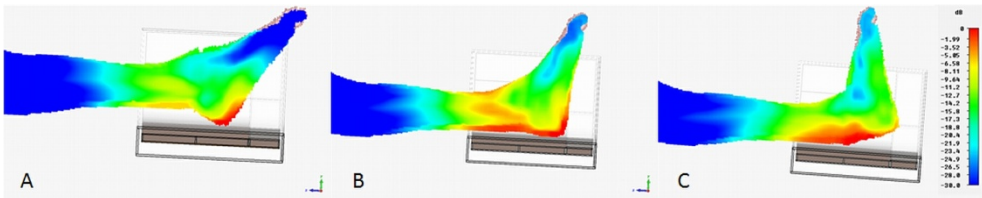

Figure 2.2: *10g-averaged SAR distribution for three different ankle postures using a dB scale normalized to the maximum at 1 W accepted input power: A) 4.73 W/kg, B) 2.28 W/kg, C) 2.61 W/kg.*

Phantom measurements

Figure 2.3 A) and B) show the measured relative SNR maps. They reveal that the SNR is more or less constant over the 15 cm length of the array. The SNR drops to about 25% at the center of the phantom relative to the surface.

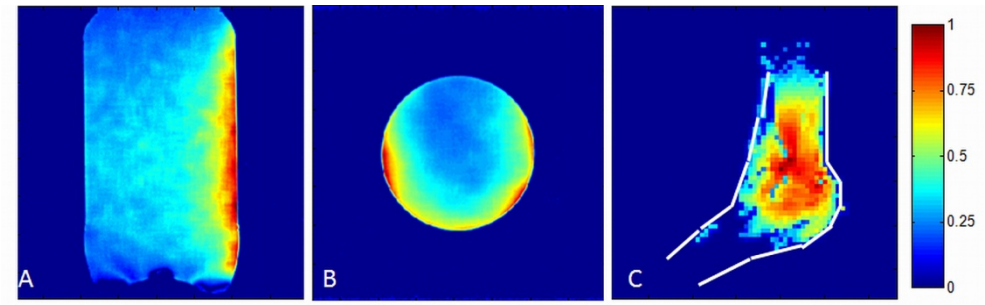

Figure 2.3: *A) and B) show relative SNR distributions in a saggital and an axial section of a homogeneous phantom. C) shows an in vivo B1 map. The contour of the foot is indicated by the white lines. The maximum B1 corresponds to 8 µT.*

B1 mapping

Figure 2.3 C) shows a B1 map acquired with the actual flip angle method. The maximum value is 8 µT. The distribution shows a 20% deviation over a length of 10 cm in the head-feet direction.

GRAPPA g-factor

Figure 2.4 shows GRAPPA g-factor maps from the pseudo multi replica method with nominal acceleration factors of R = 2, 3, and 4, which led to effective acceleration factors of 1.78, 2.4, and 2.91 after consideration of the reference lines. The maps clearly show that even for a nominal acceleration factor of 4 in the anterior-posterior direction, the maximum g-factor stays well below 2. The

mean values within the section for R = 2, 3, and 4 are 1.02, 1.12, and 1.37, respectively.

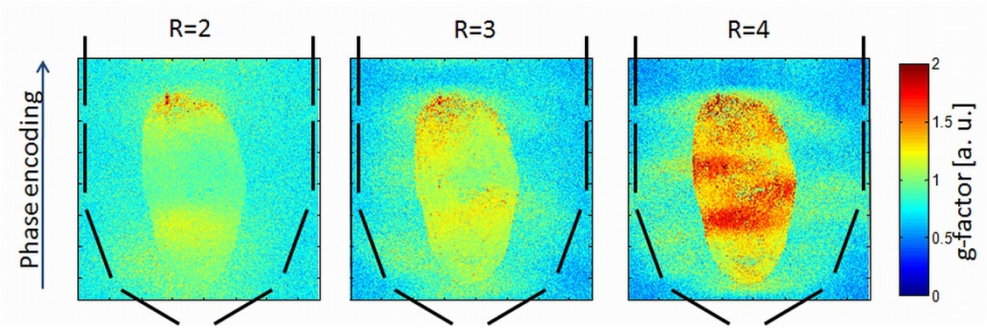

Figure 2.4: *In vivo pseudo multi replica g-factor maps for nominal GRAPPA acceleration factors of R = 2, 3, and 4 with phase encoding in the anterior-posterior direction. The positions of the coil elements are indicated by the black bars. The effective acceleration factors are 1.78, 2.4, and 2.91, and the mean g-factor values within the subject were found to be 1.02, 1.12, and 1.37, respectively.*

In vivo imaging: static

Figure 2.5 shows example in vivo images acquired with the coil. (A) and (B) show axial TSE images through the ankle joint. (C) displays an axial slice through the distal tibia from a 3D DESS showing a diffuse hypertrophy of the subcutaneous fat without disturbing susceptibility artifacts. (D-F) present reformatted 3D FLASH images depicting the trabecular structure of the bones as well as the fibers of the peroneal and the Achilles tendon with high contrast. Images in all three volunteers achieved good overall image homogeneity with the pre-calculated B_1 shim in the region of interest.

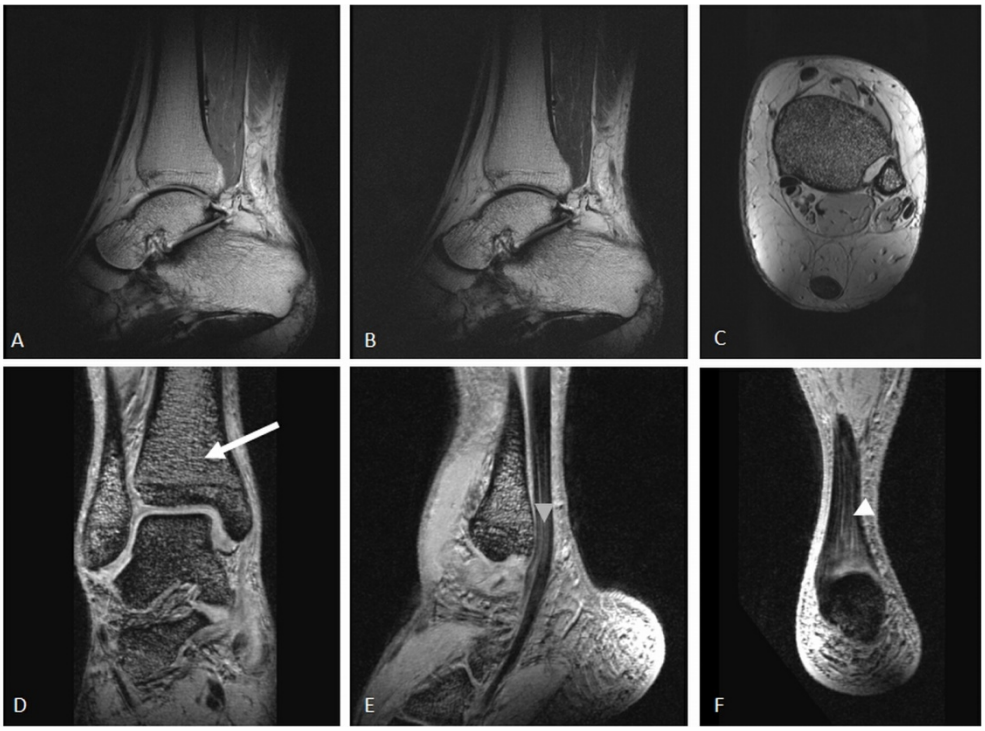

Figure 2.5: *Static images of the human ankle: (A-B) PD/T2-weighted TSE through the ankle joint; (C) axial slice through the distal tibia from a 3D DESS showing a diffuse hypertrophy of the subcutaneous fat without disturbing susceptibility artifacts, (D-F) reformatted 3D FLASH images showing the trabecular structure of the bones (arrow) as well as the fibers of the peroneal (grey arrowhead) and the Achilles tendon (white arrowhead) with high contrast.*

In vivo imaging: real-time

Figure 2.6 shows exemplary images extracted from the two real-time sequences TrueFISP (A) and TurboFlash (B) of the human ankle during free movement at a nominal imaging acceleration factor of 4. The subjects were asked to move the foot slowly for about 30 seconds during completing 5-7 cycles of motion during that time. The TrueFISP, which acquires 2.5 images per second,

revealed B_0 banding artifacts which became more severe during movement away from the initial positioning in which it was B_0-shimmed statically. The TurboFlash, which acquires 3 images per second, has intrinsically less contrast than the TrueFISP, but it did not reveal any artifacts.

All 3 subjects tolerated the total examination time of 40 minutes well. In the post-examination questioning, no complaints were reported regarding comfort of the coil.

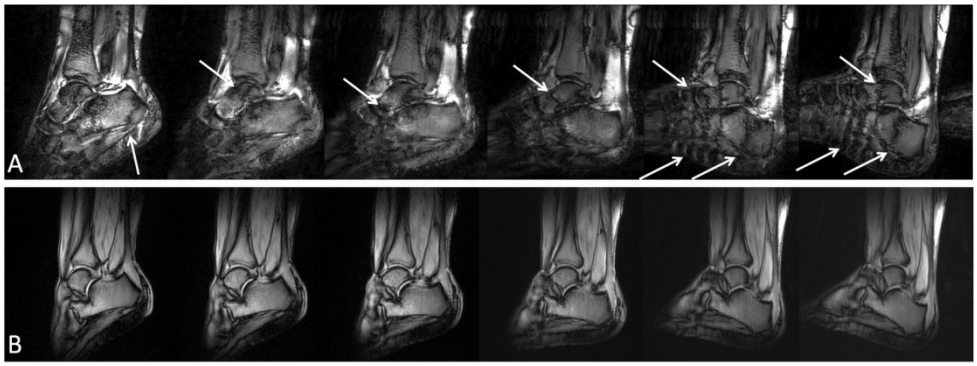

Figure 2.6: *Real-time images of the human ankle in motion. (A) TrueFISP, (B) TurboFlash at 2.5 and 3 images per second, respectively. The TrueFisp images show severe banding artifacts (arrows) which vary with the different positions of the ankle. While the TurboFlash images have an intrinsically lower contrast, they are not as sensitive to B_0 inhomogeneities.*

2.4 Discussion

The U-shaped array showed good performance with regard to patient comfort and image quality. Utilizing both parallel transmission and reception, in this work using static RF shimming and GRAPPA reconstruction, reasonable image homogeneity and high acceleration were feasible with this practical, easy access, non cylindrical transmit and receive coil arrangement.

B_1 mapping and relative SNR measurements showed good homogeneity within a field of view that is large enough to cover the ankle joint and the surrounding tissue. Patient safety was assured by simulations that covered a range of postures during patient movement. The results indicated that care has to be taken regarding movement within local transmit coils, since local SAR can vary significantly. In this particular example, the local SAR varied by a factor of approximately 2.

High-resolution imaging as well as real-time imaging were possible. Due to the low g-factor, high-resolution static images can be acquired in a clinically acceptable short time as expected considering the results in Banerjee et al. [12].

Real-time imaging with TrueFISP proved to be challenging at 7 T due to the severe banding artifacts, which has also been observed in initial cardiac applications at 7T [20]. These banding artifacts are common to this type of sequence but are more pronounced at higher field strengths. To overcome this problem, dynamic B_0 shimming [21] during ankle movement will probably have to be employed. Until this problem can be solved, TurboFlash imaging is a better alternative even though it has intrinsically lower contrast. For both sequences the parameters were chosen to achieve a good balance between spatial and temporal resolution. Nevertheless, the maximum matrix allowed by the scanner software was used to minimize the in-plane voxel size which is restricted by gradient performance. Through-plane resolution was kept at 4 mm to maintain the SNR. The temporal resolution can be made higher by sacrificing in-plane resolution or increasing the parallel imaging acceleration factor R (not currently feasible in 2D due to restrictions in the vendor software). However, the temporal resolution was

considered to be more than satisfying, as for typical ankle movement velocity non-blurred images could be obtained.

The design of the array potentially makes it suitable for hand and wrist imaging, or for imaging the knee in slender subjects. It might even be suitable for imaging larger rodents like large rats or even rabbits. The open U-shape of the proposed array would provide easier access to the animals inside the coil than closed cylindrical coils do.

2.5 Conclusion

The advancement of parallel techniques for high-field MRI has driven the need to develop dedicated coils with multiple elements for both transmission and reception. We present a U-shaped 8-channel transmit-receive array for imaging of the human ankle capable of high-resolution static imaging and real-time imaging with high acceleration factors. We have shown that real-time 2D imaging of the moving ankle joint is feasible with high spatial and temporal resolution at 7 T using nominal parallel acceleration factors up to 4.

References

1. K. P. Pruessmann, M. Weiger, M. B. Scheidegger, and P. Boesiger, "SENSE: sensitivity encoding for fast MRI," Magn Reson Med **42**, 952 (1999).

2. M. A. Griswold, P. M. Jakob, R. M. Heidemann, M. Nittka, V. Jellus, J. Wang, B. Kiefer, and A. Haase, "Generalized autocalibrating partially parallel acquisitions (GRAPPA)," Magn Reson Med **47**, 1202 (2002).

3. F. Wiesinger, P. Boesiger, and K. P. Pruessmann, "Electrodynamics and ultimate SNR in parallel MR imaging," Magn Reson Med **52**, 376 (2004).

4. M. A. Ohliger, A. K. Grant, and D. K. Sodickson, "Ultimate intrinsic signal-to-noise ratio for parallel MRI: electromagnetic field considerations," Magn Reson Med **50**, 1018 (2003).

5. U. Katscher, P. Bornert, C. Leussler, and J. S. van den Brink, "Transmit SENSE," Magn Reson Med **49**, 144 (2003).

6. W. Grissom, C. Y. Yip, Z. Zhang, V. A. Stenger, J. A. Fessler, and D. C. Noll, "Spatial domain method for the design of RF pulses in multicoil parallel excitation," Magn Reson Med **56**, 620 (2006).

7. C. M. Collins, W. Liu, B. J. Swift, and M. B. Smith, "Combination of optimized transmit arrays and some receive array reconstruction methods can yield homogeneous images at very high frequencies," Magn Reson Med **54**, 1327 (2005).

8. W. Mao, M. B. Smith, and C. M. Collins, "Exploring the limits of RF shimming for high-field MRI of the human head," Magn Reson Med **56**, 918 (2006).

9. G. Adriany, P. F. Van de Moortele, F. Wiesinger, S. Moeller, J. P. Strupp, P. Andersen, C. Snyder, X. Zhang, W. Chen, K. P. Pruessmann, P. Boesiger, T. Vaughan, and K. Ugurbil, "Transmit and receive transmission line arrays for 7 Tesla parallel imaging," Magn Reson Med **53**, 434 (2005).

10. G. Adriany, P. F. Van de Moortele, J. Ritter, S. Moeller, E. J. Auerbach, C. Akgun, C. J. Snyder, T. Vaughan, and K. Ugurbil, "A geometrically adjustable 16-channel transmit/receive transmission line array for improved RF efficiency and parallel imaging performance at 7 Tesla," Magn Reson Med **59**, 590 (2008).

11. H. H. Quick, M. E. Ladd, M. Hoevel, S. Bosk, J. F. Debatin, G. Laub, and T. Schroeder, "Real-time MRI of joint movement with trueFISP," J Magn Reson Imaging **15**, 710 (2002).

12. S. Banerjee, R. Krug, J. Carballido-Gamio, D. A. Kelley, D. Xu, D. B. Vigneron, and S. Majumdar, "Rapid in vivo musculoskeletal MR with parallel imaging at 7T," Magn Reson Med **59**, 655 (2008).

13. R. R. Regatte and M. E. Schweitzer, "Novel contrast mechanisms at 3 Tesla and 7 Tesla," Semin Musculoskelet Radiol **12**, 266 (2008).

14. X. Zhang, K. Ugurbil, R. Sainati, and W. Chen, "An inverted-microstrip resonator for human head proton MR imaging at 7 tesla," IEEE Trans Biomed Eng **52**, 495 (2005).

15. A. Christ, W. Kainz, E. G. Hahn, K. Honegger, M. Zefferer, E. Neufeld, W. Rascher, R. Janka, W. Bautz, J. Chen, B. Kiefer, P. Schmitt, H. P. Hollenbach, J. Shen, M. Oberle, D. Szczerba, A. Kam, J. W. Guag, and N. Kuster, "The Virtual Family--development of surface-based anatomical models of two adults and two children for dosimetric simulations," Phys Med Biol **55**, N23 (2010).

16. A. K. Bitz, I. Brote, S. Orzada, O. Kraff, S. Maderwald, H.H. Quick, P. Yazdanbakhsh, K. Solbach, A. Bahr, T. Bolz, K. Wicklow, F. Schmitt, and M. E. Ladd, "An 8-channel add-on RF shimming system for whole-body 7 Tesla MRI including real-time SAR monitoring," presented at the 17th Annual Meeting of ISMRM, Honolulu, HI, USA, April 18-24 (2009).

17. M. J. Firbank, A. Coulthard, R. M. Harrison, and E. D. Williams, "A comparison of two methods for measuring the signal to noise ratio on MR images," Phys Med Biol **44**, N261 (1999).

18. V. L. Yarnykh, "Actual flip-angle imaging in the pulsed steady state: a method for rapid three-dimensional mapping of the transmitted radiofrequency field," Magn Reson Med **57**, 192 (2007).

19. P. M. Robson, A. K. Grant, A. J. Madhuranthakam, R. Lattanzi, D. K. Sodickson, and C. A. McKenzie, "Comprehensive quantification of signal-to-noise ratio and g-factor for image-based and k-space-based parallel imaging reconstructions," Magn Reson Med **60**, 895 (2008).

20. C. J. Snyder, L. DelaBarre, G. J. Metzger, P. F. van de Moortele, C. Akgun, K. Ugurbil, and J. T. Vaughan, "Initial results of cardiac imaging at 7 Tesla," Magn Reson Med **61**, 517 (2009).

21. A. M. Blamire, D. L. Rothman, and T. Nixon, "Dynamic shim updating: a new approach towards optimized whole brain shimming," Magn Reson Med **36**, 159 (1996).

Chapter 3 RF Excitation using Time Interleaved Acquisition of Modes (TIAMO) to Address B1 Inhomogeneity in Highfield MRI*

Abstract

As the field strength and therefore the operational frequency in MRI is increased, the wavelength approaches the size of the human head/body, resulting in wave effects which cause signal decreases and dropouts.

Several multichannel approaches have been proposed to try to tackle these problems, including RF shimming, where each element in an array is driven by its own amplifier and modulated with a certain (constant) amplitude and phase relative to the other elements, and Transmit SENSE, where spatially tailored RF pulses are used.

In this paper a relatively inexpensive and easy to use imaging scheme for 7 Tesla imaging is proposed to mitigate signal voids due to B_1^+ field inhomogeneity. Two time-interleaved images are acquired using a different excitation mode for each. By forming virtual receive elements, both images are reconstructed together using GRAPPA to achieve a more homogeneous image, with only small SNR and SAR penalty in head and body imaging at 7 Tesla.

*__Orzada S__, Maderwald S, Poser BA, Bitz AK, Quick HH, Ladd ME.
"RF excitation using time interleaved acquisition of modes (TIAMO) to address B1 inhomogeneity in high-field MRI"
Magn Reson Med., 2010;64(2):327-333.

3.1 Introduction

Since the beginning of magnetic resonance imaging (MRI), there has been a steady drive to higher magnetic field strengths to increase signal-to-noise ratio (SNR) and to achieve new contrasts. Since operational frequency is proportional to field strength, severe problems are often encountered with today's high-field systems regarding homogeneity of the transmission field (1,2). As the operational frequency is increased, the wavelength approaches the size of the human head/body, resulting in wave effects which cause signal decreases and dropouts.

Several multichannel approaches have been proposed to try to tackle these problems. The most straightforward approach is static RF shimming (3,4). Each element in an array is driven by its own amplifier and modulated with a certain (constant) amplitude and phase relative to the other elements; the pulse profile for each element remains, however, identical. By choosing the amplitudes and phases properly, a more homogeneous transmit field or signal improvement in a certain region of interest can be achieved (5). For this approach one needs to know the transmission profiles of each element; furthermore, many channels are needed to achieve a satisfactory result (4).

A more complicated approach is Transmit SENSE (6,7), where spatially tailored RF pulses are used. Amplitude and phase vary during transmission and thus different pulse profiles are played out for each element. This approach yields excellent results, but presupposes exact knowledge of element transmission profiles as well as expensive and complicated hardware.

In this paper we propose a new imaging scheme based on multi-mode excitation and GRAPPA (8) parallel imaging reconstruction to mitigate signal voids due to B_1^+ field inhomogeneity that is relatively inexpensive and easy to apply. We designate this acquisition scheme Time-Interleaved Acquisition of Modes (TIAMO). The basic premise is to excite two (or more) different B_1^+ modes using static RF shimming in an interleaved acquisition, where the complementary RF patterns of the two modes can be exploited to improve overall signal homogeneity. Normally, this would lead to a factor two penalty in acquisition

time. However, it will be shown that the two complementary excitation modes can be viewed as forming virtual receive elements, which allows superior performance of parallel imaging algorithms over that expected from the physical receive array alone. Thus, two-fold accelerated GRAPPA encoding minimizes the scan time penalty and delivers only moderately less SNR than a conventional acquisition with a single excitation mode and full encoding, while simultaneously delivering significantly improved homogeneity in the field of view.

3.2 Theory

For a single receive coil m in conventional imaging, the spatial distribution of the signal S received by this coil m at location $\mathbf{r}$ when using a set of phases and amplitudes ("mode") n for the transmit elements in a long repetition time (TR) and short echo time (TE) gradient echo sequence using a simplified small-tip-angle approximation (9) can be approximated as

$$S_{m,n}(\mathbf{r}) \propto \hat{B}_{1,m}^{-}(\mathbf{r}) i\gamma W(\mathbf{r}) \int_0^T \hat{B}_{1,n}^{+}(\mathbf{r},t) e^{i\mathbf{r}\cdot\mathbf{k}(t)} dt \,. \qquad [3.1]$$

In this expression, W is the tissue-dependent weighting factor; $\hat{B}_{1,n}^{+}(\mathbf{r})$ and $\hat{B}_{1,m}^{-}(\mathbf{r})$ are the complex circularly-polarized components of the B_1 field, with $\hat{B}_{1,n}^{+}$ being the time-dependent combined transmit field of all coils in mode n and $\hat{B}_{1,m}^{-}$ being the receive field of coil m; γ is the gyromagnetic ratio, T is the duration of the B_1^+ pulse and $\mathbf{k}(t)$ parametrically describes a path through k-space.

Since $\hat{B}_{1,n}^{+}$ and $\hat{B}_{1,m}^{-}$ are spatially dependent, they can be described using spatial weighting factors $C_n^{+}(\mathbf{r})$ and $C_m^{-}(\mathbf{r})$:

$$S_{m,n}(\mathbf{r}) \propto C_m^{-}(\mathbf{r}) \hat{B}_1^{-} i\gamma W(\mathbf{r}) \int_0^T \hat{B}_1^{+}(t) C_n^{+}(\mathbf{r}) e^{i\mathbf{r}\cdot\mathbf{k}(t)} dt \,. \qquad [3.2]$$

$C_n^{+}(\mathbf{r})$ is time independent, so it may be extracted from the time integral and combined with $C_m^{-}(\mathbf{r})$ to a new weighting factor $C_{m,n}(\mathbf{r})$. This is mathematically equivalent to a homogeneous excitation followed by reception with a non-uniform receive sensitivity:

$$S_{m,n}(\mathbf{r}) \propto C_{m,n}(\mathbf{r}) \hat{B}_1^{-} i\gamma W(\mathbf{r}) \int_0^T \hat{B}_1^{+}(t) e^{i\mathbf{r}\cdot\mathbf{k}(t)} dt \,. \qquad [3.3]$$

This equation implies that using two different coil excitation modes in separate acquisitions is mathematically equivalent to performing one acquisition with twice the number of receive elements, each with a different reception profile. The mode excitation leads to the formation of “virtual" receive elements. Since the signal sets are acquired at different time intervals, there is no noise correlation between the two data sets.

The acquisition time needed to acquire the two different modes can be reduced back to the time to acquire a single mode by the use of parallel imaging. The requisite higher acceleration factor can be achieved thanks to the greater number of virtual receive channels. For example, two images with different excitation patterns (modes) can be acquired and reconstructed together with twice the number of “virtual” receive elements.

Although the above derivation strictly holds only in the small-tip-angle regime for long TR and short TE, our experimental results indicate that the approach also works acceptably well with high flip angles and short repetition times, as will be shown.

3.2 Materials

Scanner setup

All images were acquired on a Siemens 7T whole-body system (Magnetom 7T, Siemens Healthcare, Erlangen, Germany) using gradients with maximum amplitude of 40 mT/m and maximum slew rate of 200 mT/m/ms. The software version was VB15. For RF transmission, the vendor-provided power amplifier was used (LPPA 13080W, Dressler HF Technik GmbH, Stolberg, Germany). In conventional single-channel mode, the eight 1 kW amplifiers are combined to 8 kW with a power combiner to drive the transmit coil.

For generating arbitrary transmit modes, a custom 8-channel RF shimming system was implemented (10). In eight-channel mode, each 1 kW RF channel is independently controlled by a custom 8-channel vector modulator (11). Sets of amplitudes and phases for all channels can be buffered in the vector modulator and switched by an external trigger signal that is controlled by the sequence. The time to switch all channels to a new set of phases and amplitudes is 540 µs. During this time, no RF transmit signal should be applied since the output is undefined.

TIAMO image acquisition and reconstruction

For time-interleaved acquisition, two sets of phases with constant amplitudes are buffered in the vector modulator. The first set has a phase increment of 45° from one element to the next ("Birdcage mode"), the second set has a phase increment of 90° ("Gradient mode" or "90°-increment mode" with higher flip angle in the periphery (12)). Two images are acquired in an interleaved manner: After each acquisition line (or echo train for turbo spin echo sequences) of the first image, the same acquisition line (or echo train) for the second image is acquired. The trigger pulses were programmed into the sequences at the start of the readout of each line or at the start of the readout of the last line in the case of

an echo train. This interleaved acquisition ensures that the same line is acquired with the two modes in close temporal proximity and thus avoids inconsistencies due to motion; each line can then be interpreted as a single line with twice the number of receive channels.

Image reconstruction was performed using the 'OpenGRAPPA' (8) implementation of the GRAPPA algorithm in Matlab (The Mathworks, Natick, MA, USA). Before reconstruction, the two eight-channel raw data sets from the two different mode acquisitions were concatenated so as to form a single data matrix with a format corresponding to that of a 16-channel acquisition. This reconstruction will subsequently be referred to as 'TIAMO combined reconstruction'.

To demonstrate the advantages of the combined reconstruction method, the two mode images were also reconstructed separately using GRAPPA and subsequently combined by using the sum of squares (SoS) algorithm. This reconstruction will be referred to as 'TIAMO separate reconstruction' throughout this paper.

Coils

The coils used in this study were custom-built eight-channel transmit/receive coils. All elements are strip lines with meanders at both ends. The head coil (13) is octagonal with a minimum usable diameter of 26 cm and a strip length of 25 cm. The body array (14) used for the abdominal images consists of a dorsal section with four elements and a flexible ventral section with another four elements. Both coils were interfaced to the scanner through a set of eight transmit/receive switches and preamplifiers (Stark Contrast, Erlangen, Germany).

Phantoms

The phantom used for SNR and g-factor estimation in the head coil was a bottle with 120 mm diameter filled with tissue-simulating liquid (37.5% water, 56.5% sugar, 6% salt, ε_r = 46.3, σ = 0.8 $\Omega^{-1}\cdot m^{-1}$). Two silicon tubes were fixed longitudinally inside the bottle, one filled with the same liquid with 1:1000 Gadovist (Bayer Schering Pharma AG, Berlin, Germany) contrast agent and the other filled with air to give the phantom an inner structure. For homogeneity measurements, a phantom with the same properties was used without the silicon tubes.

Homogeneity measurement

The parameter $U_1\%$ as proposed by the AAPM protocol (15) was evaluated as an estimate of the homogeneity:

$$U_1\% = \left(1 - \frac{s_{\max} - s_{\min}}{s_{\max} + s_{\min}}\right) \cdot 100\% . \qquad [3.4]$$

$s_{\max}$ and $s_{\min}$ are the maximum and minimum pixel values within an axial slice in a homogeneous phantom.

SNR measurements and g-factor mapping

For SNR and g-factor (16) map estimation for GRAPPA, a turbo spin echo (TSE) sequence was used with a repetition time of 3000 ms and an echo time of 59 ms. The transmitter adjustment was performed using a vendor-provided B_1^+ mapping

sequence based on a spin echo and a stimulated echo (17) to achieve a 90° flip angle in the center of the phantom. Eight echoes were acquired per readout train. The matrix size was 384 by 384.

Using this sequence, two fully sampled TIAMO data sets were acquired with two modes each. The two transmission modes used in each TIAMO data set have a 45° phase increment (Birdcage mode) and a 90° phase increment, respectively. For comparison, the images were reconstructed in three ways: firstly, the birdcage mode acquisition of each TIAMO dataset; secondly, both modes of each TIAMO dataset were reconstructed separately (two times 8 channels per dataset) using OpenGRAPPA and then combined using sum of squares (TIAMO separate reconstruction); and thirdly, both modes were reconstructed together (16 channels in one data set) in OpenGRAPPA by forming "virtual" channels (TIAMO combined reconstruction). Undersampled data sets with reduction factors of 2, 3, 4, and 6 were generated from the fully sampled k-space data by selectively discarding lines that would not have been sampled in a direct acquisition accelerated with parallel imaging. The fully sampled data set was also reconstructed. 48 reference lines where used for GRAPPA reconstruction. The same raw data were used for all reconstruction schemes to ensure accurate comparison.

As mentioned, the above measurements were performed twice. Noise images were generated by subtracting the two images of each data set. A moving ROI of 20 by 20 pixels was used to determine the standard deviation in the noise image. The signal was determined using the same ROI in the sum of the two images. The ratio of these two measures provides an estimate of SNR for both the accelerated and the fully sampled images (18). Finally, measured g-factor maps were calculated by dividing the SNR maps of the fully sampled images by the SNR maps of the undersampled images, and then correcting the estimate by dividing by the square root of the 'effective' acceleration factor R_{eff}, which is given by

$$R_{eff} = \frac{N_{lines}}{\frac{N_{lines} - N_{reflines}}{R} + N_{reflines}} . \qquad [3.5]$$

Here N_{lines} is the number of phase-encoding lines of the fully sampled image, $N_{reflines}$ is the number of reference lines, and R is the nominal acceleration factor.

SAR calculations

Since SAR is a critical consideration for in vivo measurements, SAR calculations were performed using CST Microwave Studio (CST AG, Darmstadt, Germany). Three different body models were used: the male (DUKE) and the female model (ELLA) from the Virtual Family (19) with 2 mm resolution and 80 unique tissue types and the male model (HUGO) from the Visible Human Project (The Visible Human Project, http://vhp.ntu.edu.sg/.) with 2 mm resolution and 32 unique tissue types. The worst case across the three models for the 10g-averaged SAR was used to define the maximum permissible input power for each coil and mode, as other SAR values were not limiting.

In vivo imaging

For in vivo head imaging in a healthy male human volunteer (1.73 m, 70 kg), a TSE sequence was used with a TR of 3000 ms and a TE of 88 ms. The number of echoes in an echo train was eight. The matrix size was 256 by 256, 48 reference lines were acquired, and a nominal acceleration factor of 2 was used. For transmitter adjustment, a vendor-supplied B_1^+ mapping sequence was used. The transmitter voltage was chosen so that a 90° flip angle was reached in the center

of the head in the birdcage mode; the same setting was used for the 90° phase increment.

In vivo body measurements in a healthy male human volunteer (1.78 m, 75 kg) were done with a gradient echo sequence with a repetition time of TR = 10 ms, an echo time of TE = 4.1 ms and a bandwidth of 345 Hz/pixel. 48 reference lines were acquired and a nominal acceleration factor of R = 2 was used.

3.3 Results

Experiments in which two modes are acquired interleaved show that the 540 µs switching time of the vector modulator is sufficiently short enough to switch all channels during readout so that the output is always defined during transmit and the modes appear as expected when they are reconstructed.

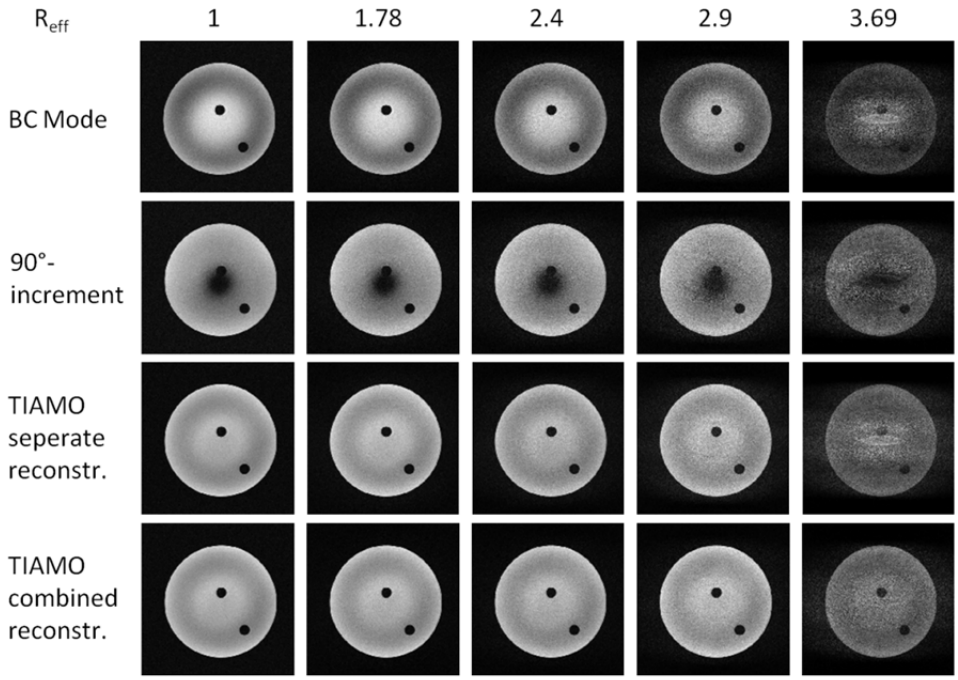

Figure 3.1: *TSE images (including the effects of both B_1^+ and B_1^- inhomogeneities) for Birdcage Mode (BC Mode, 45° phase increment), 90° phase increment, separate reconstruction with subsequent sum-of-squares combination of both modes (TIAMO separate reconstr.), and combined reconstruction of both modes (TIAMO combined reconstr.). Different effective reduction factors are shown for 48 reference lines. The nominal acceleration factors are R = 1, 2, 3, 4 and 6. The two black holes in the phantom are intentional features to provide internal structure. Please note that within a column, the TIAMO images are acquired in twice the time as the BC mode and 90°-increment mode images.*

Phantom homogeneity measurements in the head coil with the described phantom show that $U_1\%$ increases from 66.7% for the birdcage mode alone to 83.9% for the TIAMO combined reconstruction based on the two modes with 45° and 90° phase increment.

Figure 3.1 shows phantom images for the three different imaging methods and for various effective acceleration factors. The nominal acceleration factors are R = 1, 2, 3, 4, and 6. The increased homogeneity for the TIAMO method using either separate or combined reconstruction is clearly visible. The combined reconstruction also shows less pronounced residual aliasing artifacts than the other methods. Even at a nominal acceleration factor of 6 (effective 3.69), the artifacts are still acceptable in the images with the combined TIAMO method but less acceptable for the separately reconstructed original data or the separate SoS TIAMO reconstruction.

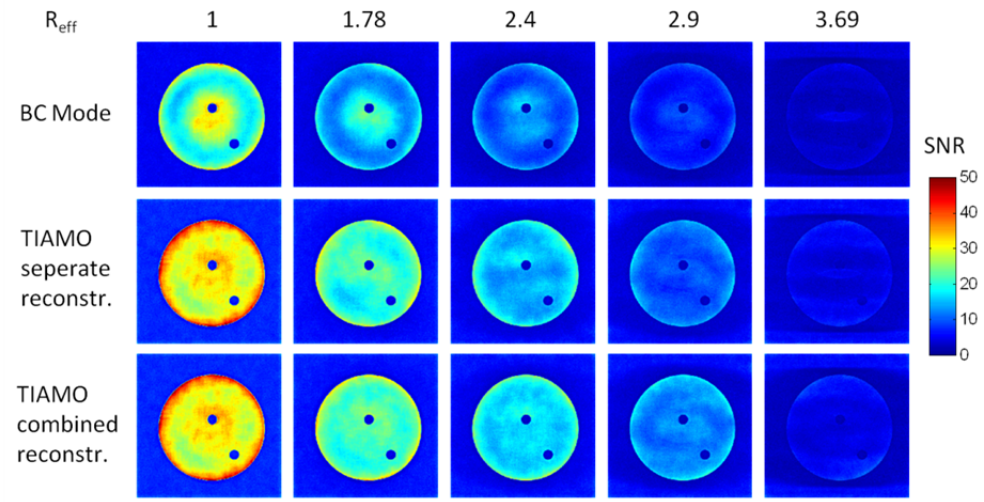

Figure 3.2: *SNR maps for Birdcage Mode (BC Mode), separate reconstruction with subsequent SoS combination of both modes (TIAMO separate reconstr.), and combined reconstruction of both modes (TIAMO combined reconstr.). Different effective reduction factors are shown. Please note that within a column, the TIAMO images are acquired in twice the time as the BC Mode images.*

The SNR maps in Figure 3.2 show that SNR is more evenly distributed when the two modes are acquired. It is also clearly evident that for exactly the same raw data, the TIAMO combined reconstruction yields a higher SNR than the separate reconstruction with subsequent SoS combination. Note that for a reduction factor R = 1, the separate and the combined TIAMO reconstructions are equivalent.

For an estimate of the increase in acquisition time with TIAMO image acquisition, Figure 3.3 shows a graph of the mean measured g-factor and the mean SNR in the phantom for the three different methods. The graphs illustrate that the TIAMO combined reconstruction is superior to the TIAMO separate reconstruction at each effective reduction factor. The mean g-factor for the birdcage mode and the TIAMO separate reconstruction are nearly the same for the lower accelerations as seen in a). The graph in b) shows, for example, that the mean SNR for the TIAMO combined reconstruction at an acceleration factor of 1.78 is the same as the mean SNR for the birdcage mode without acceleration. In this case, an effective 12% increase in acquisition time is required to achieve a considerably more evenly distributed SNR throughout the image. As TIAMO implies the doubling of the acquisition time to acquire both modes, ideally TIAMO with R_{eff} = 2 would perform equivalently to the birdcage mode without acceleration to maintain identical acquisition times. The graph reveals a 7% SNR penalty for TIAMO combined reconstruction under these conditions.

Figure 3.4 shows PD/T2-weighted in vivo head images with TIAMO acquisition (combined reconstruction). The images show increased homogeneity in the axial slice, even though an imperfection in the modes causes a slight signal drop in the left half of the brain. Especially in the T2-weighted images, an increase in the perceived detail can be noted.

Figure 3.5 shows in vivo body images with TIAMO acquisition. The coronal, sagittal, and axial planes of the T1-weighted gradient echo sequence show excellent homogeneity for 7T body imaging. No significant signal voids are seen within the coil's field of view.

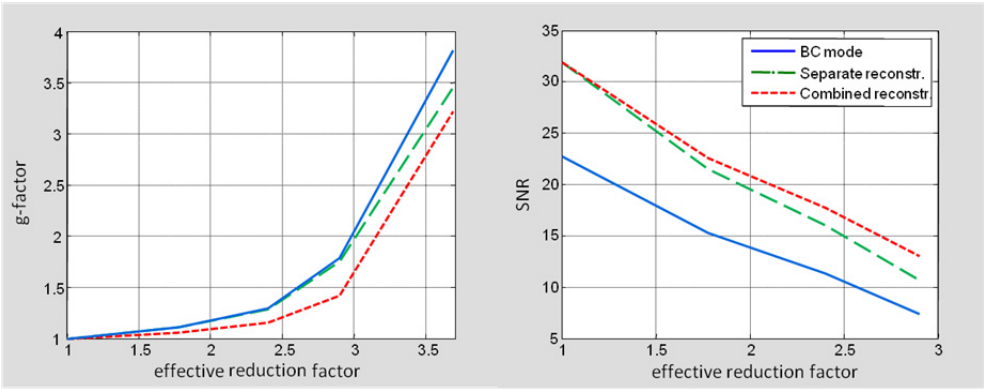

Figure 3.3: *a) Mean measured g-factor and b) mean SNR versus effective reduction factor for the three different reconstruction methods.*

SAR calculations show that the maximum permissible input power for the 90° phase increment in the head coil is 70% of that for the 45° phase increment, while in the body coil it is 89% percent. Since the modes are switched every TR, the effective permissible input power is 85% of the normal birdcage mode for the head coil and 94.5% for the body coil. Since in head imaging when using the birdcage mode the transmit amplitude is often set higher so that the flip angle in the center is greater than 90° to increase flip angle and SNR in the periphery, the SAR penalty in TIAMO may not be as severe as the decrease in permissible input power implies.

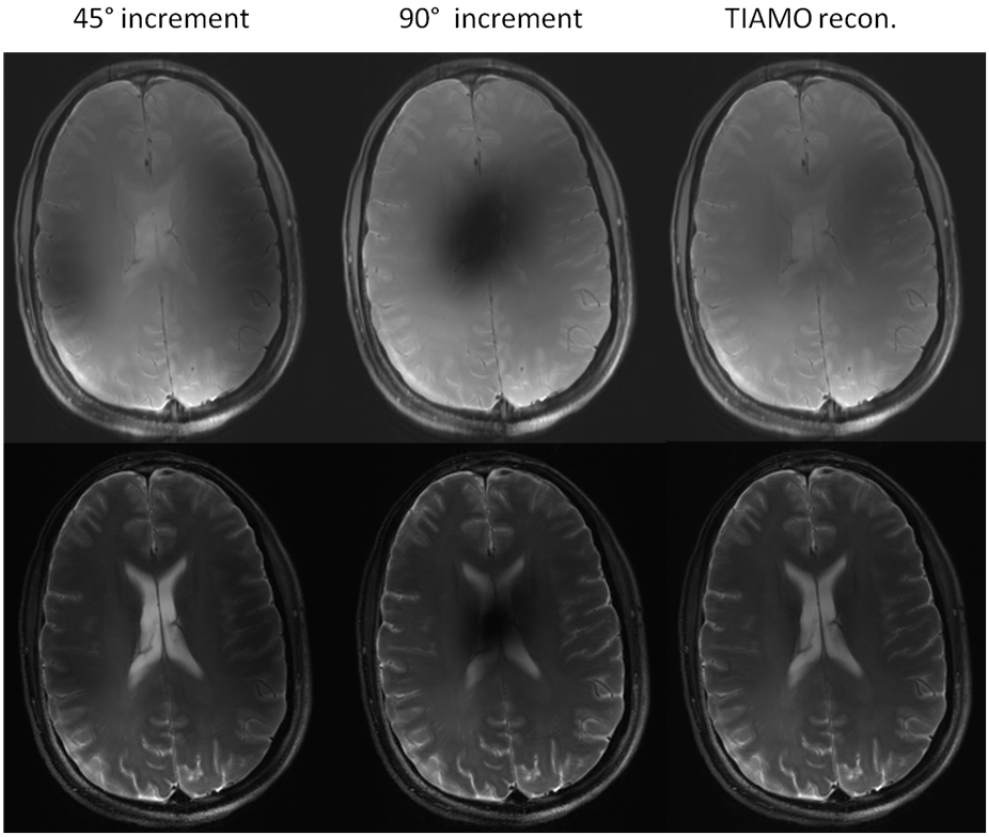

Figure 3.4: *7T PD- (top row) and T2-weighted (bottom row) TSE in vivo brain images of a human volunteer. The TIAMO images with combined reconstruction contain less signal dropout and reveal superior tissue contrast. Note: the images are not intensity corrected.*

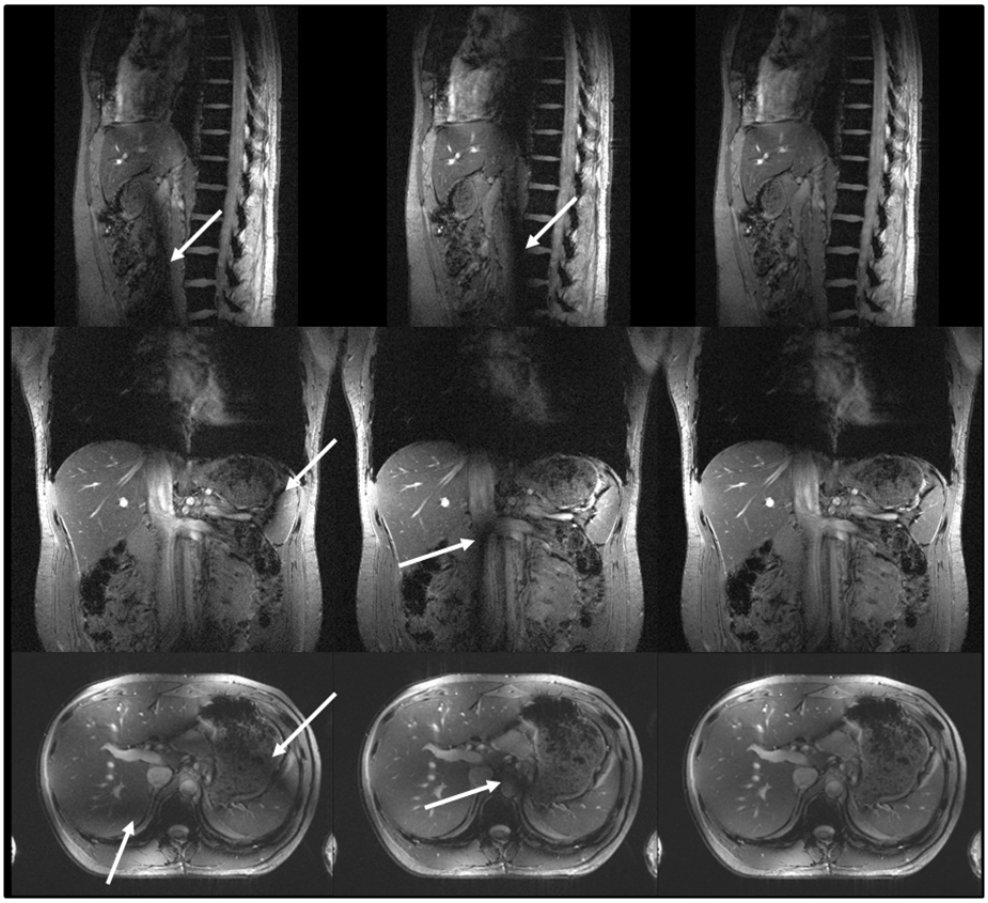

Figure 3.5: *7T T1-weighted gradient echo images in a human volunteer. The images of the two acquired modes (left and middle column) show significant signal dropouts (arrows), the images reconstructed with TIAMO combined reconstruction in the right column show no significant dropouts. Note: the images are not intensity corrected.*

3.4 Discussion

The TIAMO image acquisition method has been shown to be an easy way to mitigate signal and SNR inhomogeneities deriving from non-uniformities in the transmit B_1^+ field. Unlike specially-designed adiabatic pulses or Transmit SENSE, however, it does not aim to achieve a homogeneous transmit B_1 field per se. Rather, TIAMO attempts to effectively combine the complementary B_1^+ spatial patterns available in different RF coil modes. In contrast to adiabatic pulses or Transmit SENSE, SAR is only slightly higher than for the normal birdcage mode. The homogeneity in TIAMO reconstruction comes at the cost of either time or SNR, but this cost is kept minimal by the combined reconstruction of the virtual coil elements that are created by the different transmission modes.

It is important to note that since the B_1^+ is non-uniform in each of the individual modes, the contrast in the final image is expected to deviate from an image acquired with a uniform B_1^+ field. This would appear to make TIAMO unsuitable for most quantitative imaging, but for clinical diagnostic imaging, TIAMO might be an alternative to other ways of mitigating signal drop outs.

The required hardware is much less expensive (by approximately a factor of 5-10) than for a fully capable Transmit SENSE system, since the switching times between channel weighting values can be much longer and the synchronization is not as critical. When only using the 45° and 90° phase increment between neighboring elements, TIAMO could be implemented into a single-channel system even by the use of a simple PIN diode switch and a Butler matrix (20-22), thereby reducing the cost even further.

In conclusion, TIAMO is a simple but effective way to considerably reduce signal voids due to B_1^+ inhomogeneity in 7T head and whole-body imaging.

Future work will include optimizing the number of modes and their phase and amplitude settings to achieve optimal TIAMO images. Although only two modes were used here, the combination of three or more modes is also feasible.

References

1. Hoult DI, Phil D. Sensitivity and power deposition in a high-field imaging experiment. J Magn Reson Imaging 2000;12(1):46-67.

2. Van de Moortele PF, Akgun C, Adriany G, Moeller S, Ritter J, Collins CM, Smith MB, Vaughan JT, Ugurbil K. B(1) destructive interferences and spatial phase patterns at 7 T with a head transceiver array coil. Magn Reson Med 2005;54(6):1503-1518.

3. Collins CM, Liu W, Swift BJ, Smith MB. Combination of optimized transmit arrays and some receive array reconstruction methods can yield homogeneous images at very high frequencies. Magn Reson Med 2005;54(6):1327-1332.

4. Mao W, Smith MB, Collins CM. Exploring the limits of RF shimming for high-field MRI of the human head. Magn Reson Med 2006;56(4):918-922.

5. Metzger GJ, Snyder C, Akgun C, Vaughan T, Ugurbil K, Van de Moortele PF. Local B1+ shimming for prostate imaging with transceiver arrays at 7T based on subject-dependent transmit phase measurements. Magn Reson Med 2008;59(2):396-409.

6. Katscher U, Bornert P, Leussler C, van den Brink JS. Transmit SENSE. Magn Reson Med 2003;49(1):144-150.

7. Grissom W, Yip CY, Zhang Z, Stenger VA, Fessler JA, Noll DC. Spatial domain method for the design of RF pulses in multicoil parallel excitation. Magn Reson Med 2006;56(3):620-629.

8. Griswold MA, Jakob PM, Heidemann RM, Nittka M, Jellus V, Wang J, Kiefer B, Haase A. Generalized autocalibrating partially parallel acquisitions (GRAPPA). Magn Reson Med 2002;47(6):1202-1210.

9. Pauly J, Nishimura D, Macovski A. A k-space analysis of small-tip-angle excitation. J Magn Reson 1989;81:43-56.

10. Bitz AK, Brote I, Orzada S, Kraff O, Maderwald S, Quick HH, Yazdanbakhsh P, Solbach K, Bahr A, Bolz T, Wicklow K, Schmitt F, Ladd ME. An 8-channel add-on RF shimming system for whole-body 7 Tesla MRI including real-time SAR monitoring. In: Proceedings of the 17th Annual Meeting of ISMRM, Honolulu, HI, USA 2009; (Abstract 4767).

11. Yazdanbakhsh P, Held S, Brote I, Bitz AK, Orzada S, Ladd ME, Solbach K. 16-Bit Vector Modulator for B1 Shimming in 7T MRI. In: Proceedings of the 17th Annual Meeting of ISMRM, Honolulu, HI, USA 2009; (Abstract 4768).

12. Wiggins GC, Kraff O, Zakszewski E, Alagappan V, Wiggins CJ, Wald LL. A 7 Tesla Gradient Mode Birdcage Coil for Improved Temporal and Occipital Lobe SNR. In: Proceedings of the 14th Annual Meeting of ISMRM, Seattle, WA, USA 2006;(Abstract 214).

13. Orzada S, Kraff O, Schäfer LC, Brote I, Bahr A, Bolz T, Maderwald S, Ladd ME, Bitz AK. 8-channel transmit/receive head coil for 7 T human imaging using intrinsically decoupled strip line elements with meanders. In: Proceedings of the 17th Annual Meeting of ISMRM, Honolulu, HI, USA 2009; (Abstract 3010).

14. Orzada S, Quick HH, Ladd ME, Bahr A, Bolz T, Yazdanbakhsh P, Solbach K, Bitz AK. A flexible 8-channel transmit/receive body coil for 7 T human imaging. In: Proceedings of the 17th Annual Meeting of ISMRM, Honolulu, HI, USA 2009; (Abstract 2999).

15. Price RR, Axel L, Morgan T, Newman R, Perman W, Schneiders N, Selikson M, Wood M, Thomas SR. Quality assurance methods and phantoms for magnetic resonance imaging: report of AAPM nuclear magnetic resonance Task Group No. 1. Med Phys 1990;17(2):287-295.

16. Pruessmann KP, Weiger M, Scheidegger MB, Boesiger P. SENSE: sensitivity encoding for fast MRI. Magn Reson Med 1999;42(5):952-962.

17. Akoka S, Franconi F, Seguin F, Le Pape A. Radiofrequency map of an NMR coil by imaging. Magn Reson Imaging 1993;11(3):437-441.

18. Firbank MJ, Coulthard A, Harrison RM, Williams ED. A comparison of two methods for measuring the signal to noise ratio on MR images. Physics in medicine and biology 1999;44(12):N261-264.

19. Christ A, Kainz W, Hahn EG, Honegger K, Zefferer M, Neufeld E, Rascher W, Janka R, Bautz W, Chen J, Kiefer B, Schmitt P, Hollenbach HP, Shen J, Oberle M, Szczerba D, Kam A, Guag JW, Kuster N. The Virtual Family--development of surface-based anatomical models of two adults and two children for dosimetric simulations. Physics in medicine and biology 2010;55(2):N23-38.

20. Butler J, Lowe R. Beam forming matrix simplifies design of electronically scanned antennas. Electron Design 1961;9:170.

21. Yazdanbakhsh P, Bitz AK, Orzada S, Kraff O, Ladd ME, Solbach K. Planar Butler Matrix Technology for 7 Tesla MRI. In: Proceedings of the 17th Annual Meeting of ISMRM, Honolulu, HI, USA 2009;(Abstract 3018).

22. Alagappan V, Nistler J, Adalsteinsson E, Setsompop K, Fontius U, Zelinski A, Vester M, Wiggins GC, Hebrank F, Renz W, Schmitt F, Wald LL. Degenerate mode band-pass birdcage coil for accelerated parallel excitation. Magn Reson Med 2007;57(6):1148-1158.

Chapter 4 Time Interleaved Acquisition of Modes (TIAMO): an Analysis of SAR and Image Contrast Implications*

Abstract

As the field strength and therefore the operational frequency in MRI is increased, the wavelength approaches the size of the human head/body, resulting in wave effects which cause signal decreases and dropouts. Especially whole-body imaging at 7 Tesla and higher is therefore challenging.

Recently, an acquisition scheme called Time-Interleaved Acquisition of Modes (TIAMO) has been proposed to tackle the inhomogeneity problems in high-field MRI. The basic premise is to excite two (or more) different B_1^+ modes using static RF shimming in an interleaved acquisition, where the complementary RF patterns of the two modes can be exploited to improve overall signal homogeneity.

In this work, the impact of TIAMO on image contrast as well as on time-averaged SAR is addressed in detail. TIAMO is superior in B_1^+ homogeneity compared to conventional RF shimming while being highly SAR efficient. TIAMO can enable almost homogeneous high-field imaging throughout the entire field of view in PD, T2 and T2*-weighted imaging and, if a specified homogeneity criterion is met, in T1-weighted imaging as well.

*__Orzada S__, Maderwald S, Poser BA, Johst S, Kannengiesser S, Ladd ME, Bitz AK. "Time-Interleaved Acquisition of Modes: An Analysis of SAR and Image Contrast Implications"
Magn Reson Med., 2012;67(4):1033-1041.

4.1 Introduction

Since the early days of magnetic resonance imaging, a steady drive to higher field strengths has been apparent. At higher field strengths an increased signal-to-noise ratio (SNR) and new contrasts can be obtained, but high static field strengths of 7 Tesla and above lead to severe radiofrequency homogeneity problems (1,2) because the operational frequency is proportional to the static field strength and hence the wavelength is shortened. Especially whole-body imaging at 7 Tesla and higher is therefore challenging (3). Multichannel transmit approaches to tackle these problems have been proposed in the literature. The most notable are static RF shimming (4,5) and Transmit SENSE (6).

In RF shimming, each element in an array is driven with its own constant amplitude and phase, while the pulse profile is identical for all elements. By choosing a suitable set of amplitudes and phases, the resulting B_1^+ can be shaped within certain limitations to achieve a more homogeneous field excitation in an extended area or a localized field of view (5,7).

Transmit SENSE and equivalent approaches (8) use spatially tailored RF pulses. The amplitude and phase of each element in a transmit array are varied during transmission, leading to element-dependent pulse profiles. This approach yields excellent results, but presupposes precise knowledge of element transmission profiles as well as expensive and complicated hardware.

Recently, an acquisition scheme called Time-Interleaved Acquisition of Modes (TIAMO) (9) has been proposed to tackle the inhomogeneity problems in high-field MRI. The basic premise is to excite two (or more) different B_1^+ modes using static RF shimming in an interleaved acquisition, where the complementary RF patterns of the two modes can be exploited to improve overall signal homogeneity. The cost in time for acquiring a multitude of images can at least partly be compensated by using the multiple transmit modes to form virtual elements for a GRAPPA (10) reconstruction. Therefore, higher parallel imaging acceleration factors become feasible in conjunction with TIAMO. A first set of nearly homogeneous 7 Tesla body images were shown in (9).

Certain aspects of TIAMO remain to be investigated. For instance, since the B_1^+ distributions of the individual utilized modes are inhomogeneous, the contrast in the final image is expected to deviate from an image acquired with a uniform B_1^+ field.

With respect to power deposition in the exposed body region, it is also expected that TIAMO will likely produce a lower time-averaged specific absorption rate (SAR) than either of the utilized modes, because the different power loss densities of the alternately applied excitation modes result in a smoothed overall SAR distribution.

In this work, the impact of TIAMO on the image contrast as well as on the time-averaged SAR is addressed in detail. The image contrast is investigated with an MR experiment using a checkerboard phantom, whereas numerical experiments are carried out to compare TIAMO versus conventional single-mode RF shimming with respect to B_1^+ homogeneity and SAR at 7 Tesla. These experiments are conducted on three numerical models with inhomogeneous tissue properties for both a head and a torso coil.

4.2 Materials and Methods

Evaluation of localized SAR and B_1^+ homogeneity

For the SAR and homogeneity calculations, three different human models, a male (DUKE, 70 kg, 1.74 m, 80 tissue types) and a female (ELLA, 58 kg, 1.60 m, 80 tissue types) adult model from the Virtual Family (11) and a male model (HUGO, 95 kg, 1.85 m, 32 tissue types) from the Visible Human Project (12) were used. Field distributions in all models were calculated in CST Microwave Studio (CST AG, Darmstadt, Germany) for an 8-channel head coil (13) and a flexible 8-channel body coil (14) positioned over the liver.

The calculated E- and B-fields as well as the material parameters of the models were interpolated to a 4 mm isotropic mesh and used in the following homogeneity and SAR calculations in Matlab (The Mathworks, Natick, MA, USA).

For each combination of coil and body model, 50,000 random RF shims were calculated. Additionally, all 8 circularly-polarized (CP) modes were used as reference. Also, two optimized shims were calculated, one shim with a least squares method (lsqr) and one with a magnitude least squares method (MLS). In both cases the target distribution was a homogeneous B_1^+ distribution in an axial slice in the center of each coil. Since the optimization algorithms can converge to local optima, each optimization was repeated ten times with different starting values and the best result was chosen.

Finally, a TIAMO shim using the CP^+ and the CP^{2+} modes as well as a TIAMO shim with two optimized modes were applied for the same slice in the center of the coil. The TIAMO optimized modes were calculated using a MLS method, with a homogeneous target distribution for the root sum square (RSS) of the B_1^+ of the two modes.

$$\mathbf{b}_1, \mathbf{b}_2 = \arg_{\mathbf{b}_1, \mathbf{b}_2} \min \left\{ \left\| \sqrt{\left(\mathbf{A}\mathbf{b}_1\right)^2 + \left(\mathbf{A}\mathbf{b}_2\right)^2} - \mathbf{m} \right\|^2 \right\} \qquad [4.1]$$

Here, $\mathbf{b}_1$ and $\mathbf{b}_2$ are complex column vectors with *N* elements containing the shim settings of all *N* channels for the two utilized modes, **A** is a matrix with *N* columns containing the B_1^+ of all voxels in the ROI for all *N* transmit elements, and *m* is a column vector containing the homogeneous target distribution. Please note that the squares and the square root denote element-wise operations. Eq. 1 was solved using a simplex search method (15). Again, each optimization was repeated ten times with different starting values and the best result was chosen.

As a measure of homogeneity, the standard deviation of the B_1^+ of the individual RF shims and of the RSS of the two shims in TIAMO was calculated in the axial slice in the center of each coil within the body model.

Because of the large number of investigated RF shims, a fast procedure for the estimation of the 10 g-averaged SAR (SAR_{10g}) was implemented by using a sliding cube of 20 mm edge length as the averaging volume and assuming a homogeneous tissue density of 1000 kg/m³.

SAR for TIAMO was estimated by averaging the voxel-based SAR for the two utilized modes to account for the interleaved excitation. Afterwards, the SAR_{10g} averaging scheme and the homogeneity evaluation were used as described above.

A comparison of efficiency between RF shimming and TIAMO in terms of mean B_1 amplitude in a slice versus SAR was performed based on the received signal energy over the time needed to acquire the complete information, which is the mean signal power disregarding all subsequent signal processing. In RF shimming the received signal energy is proportional to the square of B_1^+ of the RF shim, while in TIAMO it is proportional to the sum of squares (SoS) of the B_1^+ for the two modes. The time to acquire the complete TIAMO dataset is twice the duration for the conventional RF shim:

$$efficiency_{shimming} = \frac{\overline{\left|\mathbf{B}_1^+\right|^2}}{SAR_{10g} \cdot T_A} \qquad [4.2]$$

$$efficiency_{TIAMO} = \frac{\overline{\left|\mathbf{B}_{1,1}^{+}\right|^2 + \left|\mathbf{B}_{1,2}^{+}\right|^2}}{SAR_{10g} \cdot 2T_A} . \qquad [4.3]$$

Here $\mathbf{B}_{1,1}^{+}$ and $\mathbf{B}_{1,2}^{+}$ are the transmit fields of the first and second TIAMO modes, respectively, and T_A is the time to acquire a single mode. Note that the square denotes element-wise operations and the bar denotes the mean throughout all elements of the matrix.

In all simulations with numerical head models, the upper body down to the Xiphoid process of the sternum was included. In the simulations with the body coil, the trunk of each model was used. To account for realistic positioning, the small models (ELLA, DUKE) had their arms outside of the coil, whereas the bigger model (HUGO) had its arms inside the coil.

Scanner setup

All images were acquired on a Siemens 7T whole-body system (Magnetom 7T, Siemens Healthcare, Erlangen, Germany) using gradients with maximum amplitude of 40 mT/m and maximum slew rate of 200 mT/m/ms. The software version was VB15. For RF transmission, the vendor-provided power amplifier was used (LPPA 13080W, Dressler HF Technik GmbH, Stolberg, Germany). In conventional single-channel mode, the eight 1 kW amplifiers are combined to 8 kW with a power combiner to drive the transmit coil.

For generating arbitrary transmit modes, a custom 8-channel RF shimming system was implemented (16). In eight-channel mode, each 1 kW RF channel is independently controlled by a custom vector modulator (17). Sets of amplitudes and phases for all channels can be buffered in the vector modulator and switched by an external trigger signal that is controlled by the sequence. The time to switch all channels to a new set of amplitudes and phases is 540 µs. During this time, no

RF transmit signal should be applied, since the output is undefined, so the system is fast enough to perform TIAMO but not fast enough for full Transmit SENSE.

All sequences were modified by adding a trigger pulse to switch between the utilized modes after each k-space line or echo train. To enable TIAMO combined reconstruction, a software package was implemented on the scanner which restructures the incoming raw data in such a way that the N interleaved acquisitions are interpreted by the scanner's reconstruction system as N times the number of channels of a single acquisition. After this restructuring/reordering, the standard reconstruction system handles the data as usual.

Contrast measurements:

For contrast measurements, a phantom consisting of a matrix of 10 by 10 cylinders was used. The cylinders had an inner diameter of 12 mm, an outer diameter of 13.5 mm, and a length of 44 mm. They were filled in a checkerboard pattern with either water or rapeseed oil. For measurements inside the MR imager, the checkerboard phantom was placed centrally in a custom-built 8-channel head coil (13), so that the checkerboard pattern was visible in the axial slice. To provoke strong B_1 inhomogeneities, the checkerboard phantom was inserted into a water-filled canister of 15 x 15 x 20 cm^3. For comparison with a nearly homogeneous transmit field, the experiment was repeated without the water-filled canister.

The contrast measurements were performed with the CP^+ (phase increment 45°) and the CP^{2+} (phase increment 90°) mode of the coil array, and the transmitter voltage was adjusted to achieve the desired flip angle with the CP^+ mode ("birdcage mode") in the center of the phantom.

Five 2D sequences were evaluated: a T1- and a T2*-weighted FLASH sequence, a PD- and a T2-weighted Turbo Spin Echo sequence (TSE) and a T1-weighted Spin Echo (SE) sequence. All sequences had a field of view (FOV) of 200 x 200 mm^2 and

a matrix of 256 x 256 with a slice thickness of 5 mm. The bandwidths of all sequences were kept high to keep the fat/water shift below 2 pixels. A complete set of the sequence parameters can be found in Table 4.1.

	TR [ms]	TE [ms]	FA [°]	BW [Hz/pixel]	ETL
T1 FLASH	20	4.34	25	930	-
T2* FLASH	750	25	35	930	-
PD TSE	5000	6.8	90/180	780	7
T2 TSE	5000	88	90/180	780	13
T1 SE	250	6.8	90/180	780	-

Table 4.1: *Sequence parameters used for the contrast evaluation.*

The contrast was evaluated by placing a circular region of interest (ROI) in every compartment of the phantom in an axial slice acquired with each of the above-mentioned sequences. Every ROI contained about 80 pixels. The mean signal in each ROI was determined and the ratio of this signal to the mean signal from the 4 surrounding compartments filled with the other liquid was calculated to get an estimation of the contrast distribution. The standard deviation of this contrast distribution was used as a quality measure. The results from CP^+ with the phantom in air, from CP^+ and CP^{2+} with the phantom in water, as well as a TIAMO image using CP^+ and CP^{2+} were compared. Each mode was acquired twice in an interleaved way and averaged, so that the acquisition times for both the individual modes and the subsequent TIAMO scan with two interleaved modes were the same.

4.3 Results

SAR and homogeneity calculations

Figure 4.1 depicts the results for the simulations as a scatter plot. The y-axis shows the standard deviation of the mean B_1^+ in percent, the x-axis shows the efficiency. Plots A,C,E are simulated for the head coil, plots B,D,F are for the body coil. The rows represent the DUKE, ELLA, and HUGO body model from top to bottom. Since the plots in Fig. 4.1 show different body shapes and coils, a global efficiency normalization is not required. For convenience, the efficiency in each plot is normalized to the maximum of the random RF shims for that plot. The ideal case would be found in the lower right corner of each plot, representing a high efficiency and a low standard deviation (high homogeneity).

TIAMO clearly provides the lowest standard deviation while achieving a good efficiency at the same time. In head imaging, even the non-optimized TIAMO with the CP^+ and CP^{2+} modes shows a lower standard deviation than the optimized RF shims. In Figure 4.1F (HUGO, body coil), one of the optimized RF shims shows a lower standard deviation than the optimized TIAMO; however, Figure 4.2 shows that the homogeneity of the TIAMO shim is subjectively superior to the optimized RF shim.

Figure 4.2 shows comparisons of the optimized TIAMO shim and the best RF shim for all 3 models and both body regions.

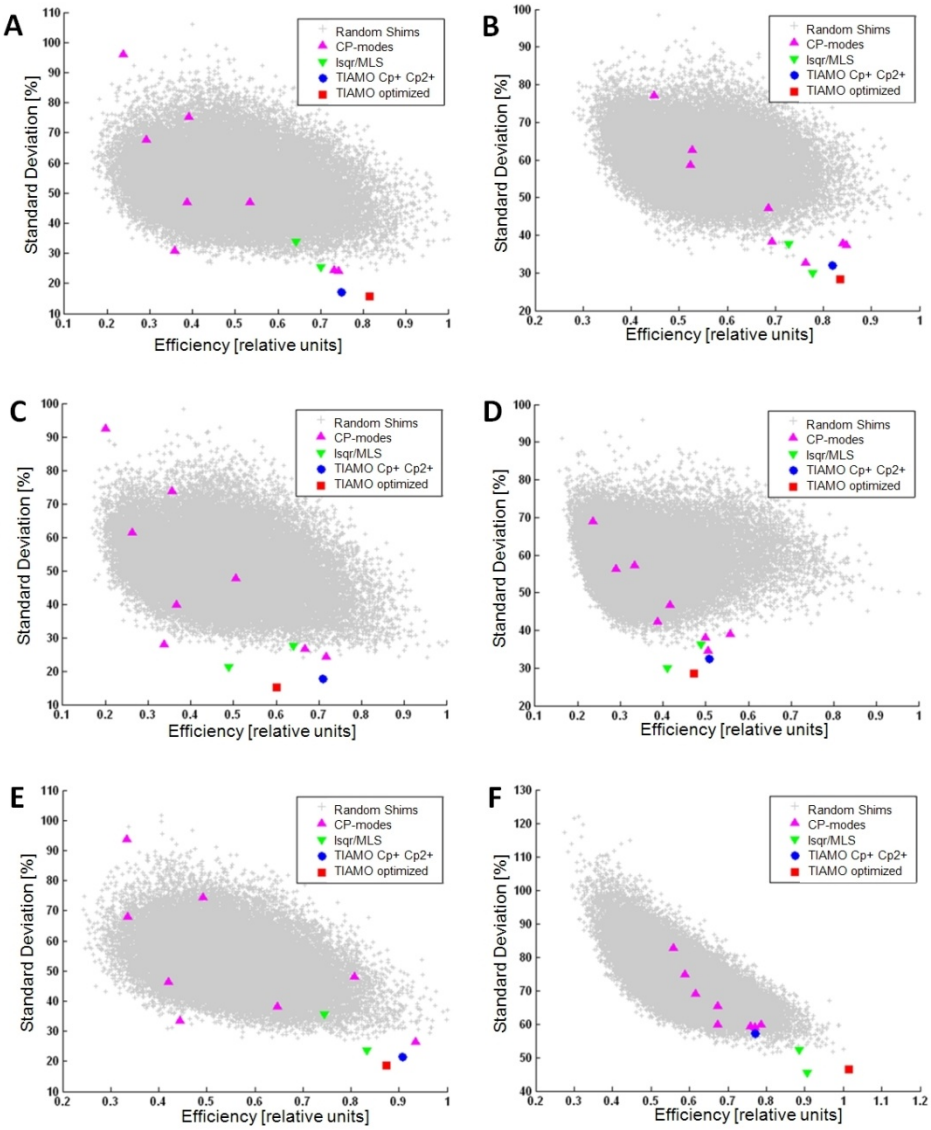

Figure 4.1: *Standard deviation versus efficiency. From top to bottom: DUKE, ELLA, HUGO. Left column shows results for the head coil, right column shows results for the body coil.*

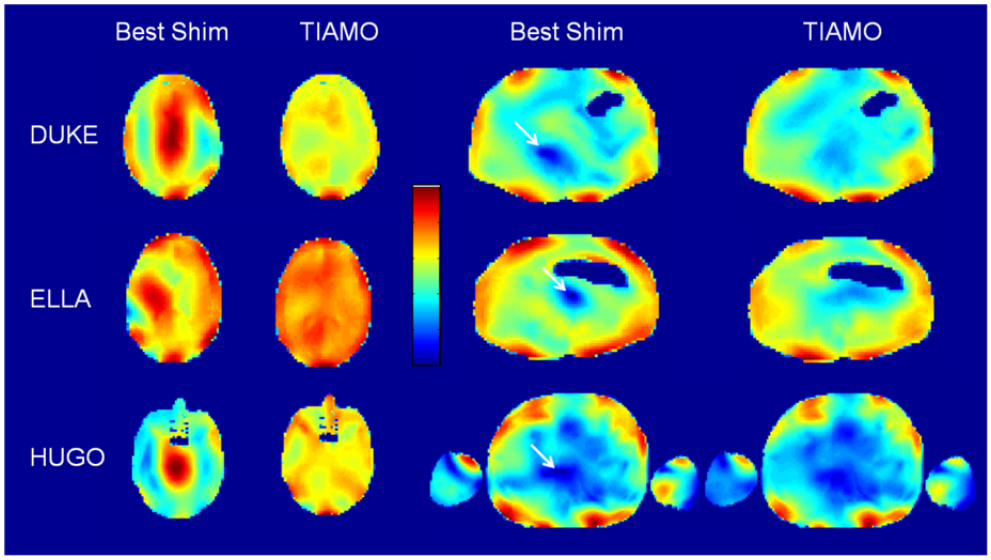

Figure 4.2: *Comparison of TIAMO and best conventional RF shims for all three body models and both RF coils. TIAMO shows superior qualitative homogeneity. The white arrows point to signal dropouts in the body coil shims. Each panel is scaled from 0 to the maximum of $|B_1^+|$ in the respective panel.*

Contrast measurements

Figure 4.3 shows the images of the checkerboard phantom for all sequences and for the following four cases: nearly homogeneous excitation by the CP^+ mode with the checkerboard phantom in air, and CP^+ mode, CP^{2+} mode, and the TIAMO acquisition composed of the CP^+ and CP^{2+} modes, the latter three with the checkerboard phantom immersed in water. Signal voids in the CP^+ and CP^{2+} modes are clearly visible.

In Table 4.2, the calculated standard deviation in percent of the contrast inside the checkerboard phantom is given for all images. The standard deviation of the CP^+ and CP^{2+} images is much higher than it is for the homogeneous excitation,

while the standard deviation in the TIAMO images approaches or is even lower than for the homogeneous excitation in some cases.

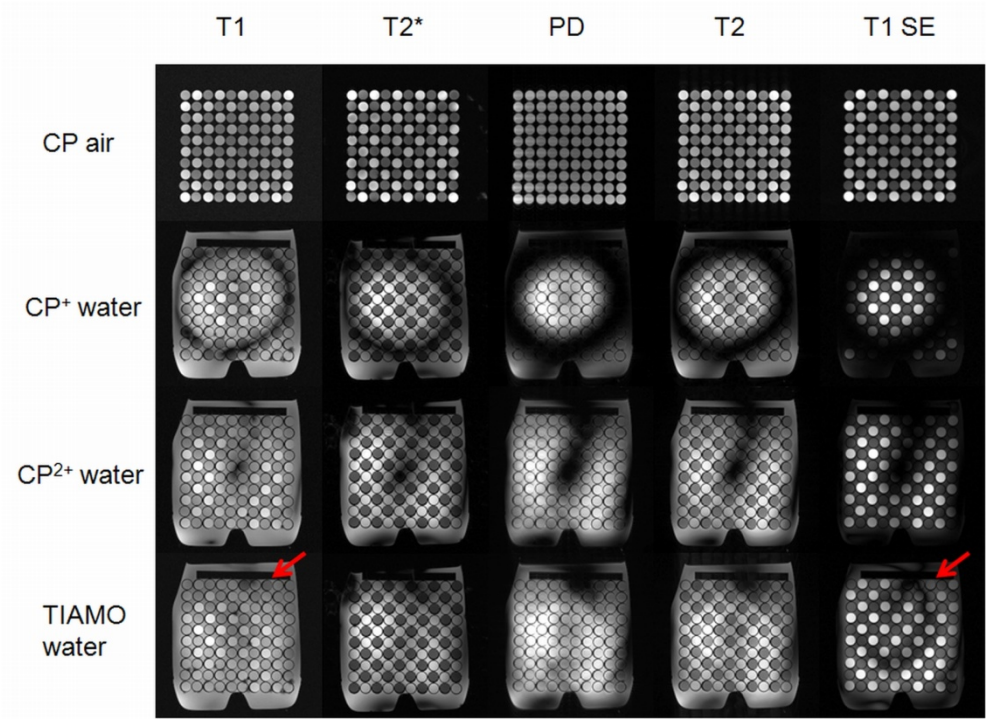

Figure 4.3: *MR images of the checkerboard phantom acquired with the 8-channel head coil. Arrows point out contrast errors in the TIAMO images*

	T1 FLASH	T2* FLASH	PD TSE	T2 TSE	T1 SE
CP^+, Air	3.1	11.7	3.5	7.0	2.8
CP^+, Water	38.5	36.4	88.8	77.0	120.3
CP^{2+}, Water	16.7	32.5	75.2	48.5	86.4
TIAMO	9.3	9.2	6.8	6.7	32.4

Table 4.2: *Standard deviation in percent of the contrast in the checkerboard phantom.*

In the T1-weighted gradient echo images (Figure 4.3, first column) for the inhomogeneous cases, contrast errors appear with partially inverse (see arrow)

contrast compared to the homogeneous case, especially in the upper row of the checkerboard phantom. In regions where the ring-shaped signal dropout of the CP^+ mode is located, different contrasts for the CP^+ and CP^{2+} modes are obvious which result in a TIAMO image with varying contrast. The standard deviation of the contrast is three times higher in the TIAMO image than for the homogeneous excitation.

In the second column, the T2* contrast looks apparently correct throughout the acquisitions with inhomogeneous excitations. Some small B_0 artifacts (blooming) caused by small bubbles of air are visible in the cases where the checkerboard phantom is immersed in the water canister. The calculated standard deviation of the contrast for the TIAMO image is almost the same as it is for the image acquired with homogeneous excitation.

In the PD-weighted TSE images in the center column, the contrast between the oil and the water is quite low. The apparent contrast does not vary much in the images with inhomogeneous excitation. The measured standard deviation in the TIAMO image is nearly doubled compared to the homogeneous excitation.

The T2 images with water immersion in the fourth column show qualitatively the same contrast as the image with homogeneous excitation. The TIAMO image appears fairly homogeneous, and the standard deviation of the contrast is almost the same as in the image with homogeneous excitation.

In the fifth column, the T1-weighted spin echo images qualitatively reveal a mostly acceptable contrast. The standard deviation for the CP^+ and CP^{2+} modes is much higher than the standard deviation in the image with homogeneous excitation. Strong deviation in the contrast can be observed in the upper right corner of the TIAMO image, where the contrast between oil and water is noticeably (see arrow) much lower than in the rest of the phantom.

In the appendix an analytical evaluation of the contrast in a TIAMO spoiled gradient echo image is given. This theoretical analysis indicates that T1 contrast is affected by the inhomogeneities of the two modes. Since the criterion for

homogeneity of the B_1^+ distribution (Eq. 1) and the criterion for homogeneous contrast distribution (cf. Eq. 11) are approximately identical, a correct T1 contrast can be achieved with TIAMO using this specific homogeneity criterion. This is demonstrated in Figure 4.4, which shows the relative B1 maps of two inhomogeneous B1 shims (A,B) and the homogenous RSS of these shims (C). The resulting image (D) shows correct T1-weighted contrast throughout the image.

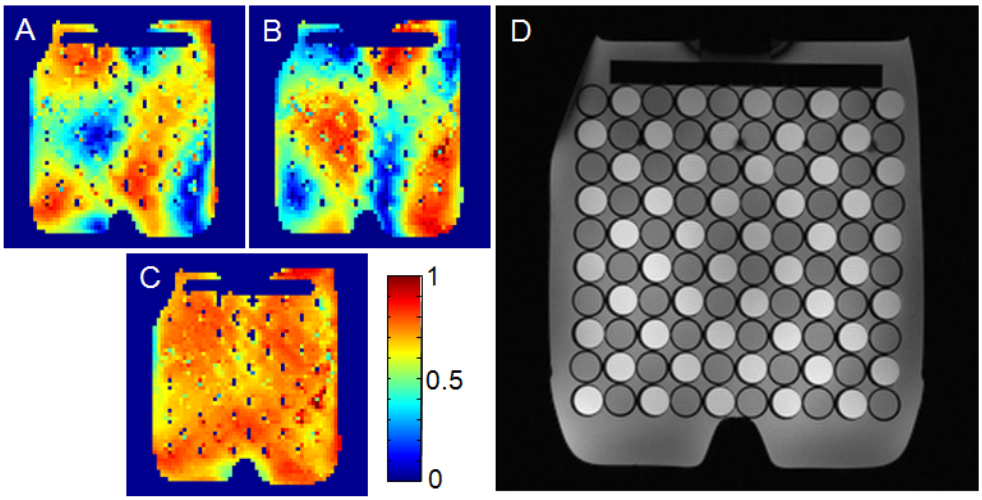

Figure 4.4: *(A) and (B) show relative B1 maps of two inhomogeneous shim sets calculated using the homogeneity criterion given in Eq. 1. (C) shows the RSS combination. (D) shows the resulting T1-weighted TIAMO image with correct contrast.*

4.4 Discussion

SAR and B_1^+ homogeneity evaluation

The results show that TIAMO is superior to RF shimming concerning image homogeneity and/or SAR efficiency. A reason for the good SAR efficiency is that the maximal SAR for the two utilized modes can appear at different locations. Thereby, the time-averaged SAR_{10g} can be significantly reduced in comparison to the SAR_{10g} of the individual modes.

The TIAMO shims in Figure 4.2 qualitatively look more homogeneous than the RF shim; also, they do not exhibit complete signal voids, whereas the best shims for the body array show at least one complete signal dropout (see arrows). In Figure 4.1F the standard deviation for the TIAMO optimized shim is higher than it is for the best conventional RF shim, but taking the signal dropout into account, the TIAMO shim seems preferable. In all three simulation models with the head coil, the non-optimized combinations of the CP^+ and CP^{2+} modes with TIAMO are already superior in homogeneity compared to the conventional RF shims. As stated in previous work (9), this combination can be easily realized with a Butler matrix (18) and a switch, making it a very cost-efficient and robust option for homogeneous head imaging.

In summary, the signal homogeneity achieved with TIAMO is higher than that which can be achieved with RF shimming. Complete signal dropouts can be avoided with TIAMO, while conventional RF shims in body imaging show at least one significant dropout. In the smaller bodies of ELLA and DUKE, the signal homogeneity achievable with TIAMO should be sufficient for human in vivo imaging. Individual TIAMO shims can significantly improve the image quality in comparison to conventional RF shimming with a limited number of channels (8 in this case). Higher channel numbers might lead to different conclusions.

Contrast measurements

As stated in previous work (9), TIAMO does not achieve a homogeneous excitation, but aims at acquiring composite images with a homogeneous signal distribution. The modes used in a TIAMO acquisition scheme are inherently inhomogeneous.

T1-weighted sequences in particular are affected by the inhomogeneities of the modes used for TIAMO. This effect is reduced significantly in T1-weighted spoiled gradient echo images if the RSS of the two flip angles (or B_1 fields) is homogeneous, which is the same criterion as for signal strength homogeneity. To get a more correct T1 contrast in spin echo imaging or in gradient echo imaging if the homogeneity criterion cannot be met, sub-image combination of consecutive scans with optimization with respect to the B_1^+ as proposed by Katscher et al. (19) could be applied, but consecutive scans imply a greater temporal spacing between the individual k-lines of the mode datasets, which can lead to increased motion sensitivity, such that the datasets might not form virtual channels of a virtual single acquisition. In cases where the correct contrast is important only in a certain organ or ROI, the shims for TIAMO might be chosen in such a way that the desired flip angle is achieved in the ROI in both modes while the signal dropouts are located in different positions outside of the ROI. In this way, the correct contrast could be achieved within the ROI, and the tissue distribution outside would still be visible without dropouts (albeit with incorrect contrast).

Measurements with long TR such as PD-, T2- and T2*-weighted sequences are not affected by the inhomogeneities of the modes. Therefore, measurements with such sequences using TIAMO will render the desired contrast.

4.5 Conclusion

The presented numerical experiments show that TIAMO is superior to conventional RF shimming with respect to B_1^+ standard deviation and perceived homogeneity in the final image. At the same time, TIAMO offers a very high SAR efficiency when compared to RF shims with similar homogeneity, since the modes used in TIAMO can have SAR hotspots in divergent locations, so that the resulting overall SAR is lower than that of an individual mode.

The experiments performed to evaluate the impact of TIAMO on basic contrast mechanisms show that sequences which target T1 contrast may be affected by B_1^+ inhomogeneities, whereas PD-, T2-, or T2*-weighted sequences using the contrast mechanisms considered in this paper are not affected. For T1-weighted spoiled gradient echo sequences, analytical analysis indicates that the correct contrast will be achieved if the RSS of the B_1^+ of the two modes is used for homogeneity optimization.

TIAMO is superior in B_1^+ homogeneity compared to conventional RF shimming while being highly SAR efficient. Therefore, TIAMO can enable almost homogeneous high-field imaging throughout the entire field of view in PD, T2, and T2* imaging, as well as in T1-weighted spoiled gradient echo imaging if the presented homogeneity criterion is met.

4.6 Appendix

In this appendix an expression for the steady-state magnetization in a TIAMO spoiled gradient echo sequence is derived and an evaluation of the impact of TIAMO on image contrast is given.

The longitudinal magnetization M_Z at the time point $(n+1)\cdot T_R$ after applying an RF pulse to achieve a flip angle θ_1 can be written as

$$M_Z((n+1)T_R) = M_Z(nT_R)\cos\theta_1 \cdot e^{-\frac{T_R}{T_1}} + M_0(1-e^{-\frac{T_R}{T_1}}) \qquad [4.4]$$

where M_0 is the equilibrium longitudinal magnetization, T_R is the repetition time, and T_1 is the longitudinal relaxation time (20). In TIAMO, another pulse is applied at time point $(n+1)T_R$ which achieves a flip angle θ_2 leading to a longitudinal magnetization of

$$M_Z((n+2)T_R) = M_Z((n+1)T_R)\cos\theta_2 \cdot e^{-\frac{T_R}{T_1}} + M_0(1-e^{-\frac{T_R}{T_1}}) \qquad [4.5]$$

For even n the steady-state magnetizations M_{ZE1} and M_{ZE2} for such a series of alternating pulses have to satisfy

$$M_Z((n+2)T_R) = M_Z(nT_R) = M_{ZE1} \text{ and} \qquad [4.6]$$

$$M_Z((n+3)T_R) = M_Z((n+1)T_R) = M_{ZE2} \qquad [4.7]$$

This yields the steady-state magnetization values for the two modes

$$M_{ZE1} = \frac{M_0 \cdot (1-e^{-\frac{T_R}{T_1}}) \cdot (1+e^{-\frac{T_R}{T_1}} \cdot \cos\theta_2)}{1-\cos\theta_1 \cdot e^{-\frac{2T_R}{T_1}} \cdot \cos\theta_2} \qquad [4.8]$$

$$M_{ZE2} = \frac{M_0 \cdot (1 - e^{-\frac{T_R}{T_1}}) \cdot (1 + e^{-\frac{T_R}{T_1}} \cdot \cos\theta_1)}{1 - \cos\theta_1 \cdot e^{-\frac{2T_R}{T_1}} \cdot \cos\theta_2} \qquad [4.9]$$

The steady-state signal S of a voxel containing several isochromats (20) in the combined image is the RSS of the signals from the two modes:

$$S \propto \rho_0 \cdot e^{-\frac{T_E}{T_2^*}} \cdot \frac{\left(1 - e^{-\frac{T_R}{T_1}}\right) \sqrt{\sin^2\theta_1 \cdot \left(1 + \cos\theta_2 \cdot e^{-\frac{T_R}{T_1}}\right)^2 + \sin^2\theta_2 \cdot \left(1 + \cos\theta_1 \cdot e^{-\frac{T_R}{T_1}}\right)^2}}{1 - \cos\theta_1 \cdot \cos\theta_2 \cdot e^{-\frac{2T_R}{T_1}}} \qquad [4.10]$$

Here ρ_0 is the voxel spin density, T_E denotes the echo time, and T_2^* is the effective transverse relaxation time.

To evaluate the influence of TIAMO on contrast, the ratio of the signals from two tissues with different ρ_0, T_1 and T_2^* is:

$$\frac{S_1}{S_2} = \frac{\rho_{0,1}}{\rho_{0,2}} \cdot \frac{e^{-\frac{T_E}{T_{2,1}^*}}}{e^{-\frac{T_E}{T_{2,2}^*}}} \cdot \frac{\dfrac{\left(1 - e^{-\frac{T_R}{T_{1,1}}}\right) \cdot \sqrt{\sin^2\theta_1 \cdot \left(1 + \cos\theta_2 \cdot e^{-\frac{T_R}{T_{1,1}}}\right)^2 + \sin^2\theta_2 \cdot \left(1 + \cos\theta_1 \cdot e^{-\frac{T_R}{T_{1,1}}}\right)^2}}{1 - \cos\theta_1 \cdot \cos\theta_2 \cdot e^{-\frac{2T_R}{T_{1,1}}}}}{\dfrac{\left(1 - e^{-\frac{T_R}{T_{1,2}}}\right) \cdot \sqrt{\sin^2\theta_1 \cdot \left(1 + \cos\theta_2 \cdot e^{-\frac{T_R}{T_{1,2}}}\right)^2 + \sin^2\theta_2 \cdot \left(1 + \cos\theta_1 \cdot e^{-\frac{T_R}{T_{1,2}}}\right)^2}}{1 - \cos\theta_1 \cdot \cos\theta_2 \cdot e^{-\frac{2T_R}{T_{1,2}}}}}$$

[4.11]

The first fraction represents the proton density contrast, the second fraction represents the $T2^*$ contrast, and the third fraction, C_{T1}, represents the T1 contrast. If T_R is chosen sufficiently large, the influence of the flip angle on image contrast in TIAMO is negligible. It is evident, however, that the T1 contrast is dependent on both flip angles θ_1 and θ_2. C_{T1} is approximately constant if the sum of squares of

the two flip angles is constant and in the range of 0 to 90°. Within the whole parameter space $T_{1,1}, T_{1,2}, T_R \in [0, \infty]$, the standard deviation of C_{T1} on any quarter circle representing a constant RSS of the flip angles is below 6% and the peak normalized error ($[C_{T1,max} - C_{T1,min}] / [C_{T1,max} + C_{T1,min}]$) error is approximately 8%. Figure 4.5 plots an example for C_{T1} with TR of 200 ms and materials with T1 values of 2581 ms and 488 ms. The RSS of the flip angles being constant is equivalent to the homogeneity criterion given in equation [4.1] of the Methods section.

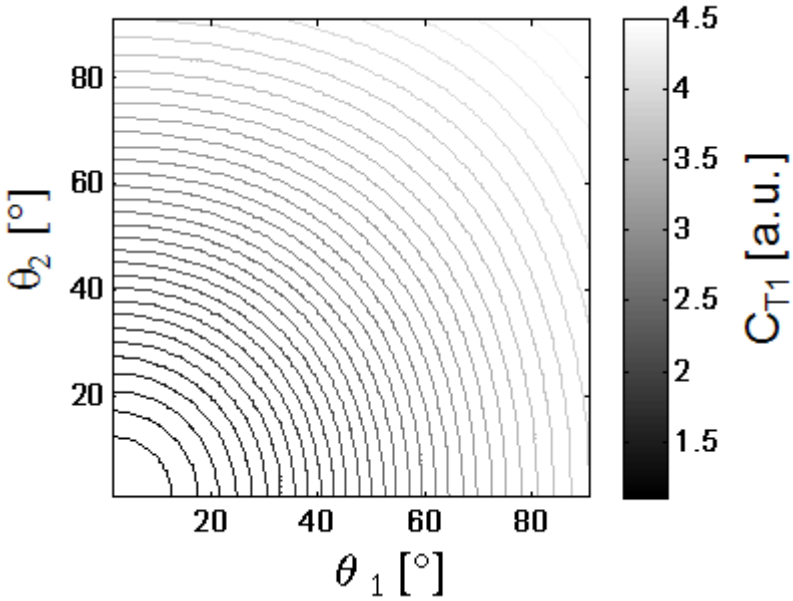

Figure 4.5: *Contour plot of the T1 contrast C_{T1} between two materials in TIAMO with T1 of 2581 ms and 488 ms at a TR of 200 ms. It is evident that the contour lines approximately follow quarter circles representing a constant RSS of the two flip angles.*

References

1. Hoult DI, Phil D. Sensitivity and power deposition in a high-field imaging experiment. J Magn Reson Imaging 2000;12(1):46-67.

2. Van de Moortele PF, Akgun C, Adriany G, Moeller S, Ritter J, Collins CM, Smith MB, Vaughan JT, Ugurbil K. B(1) destructive interferences and spatial phase patterns at 7 T with a head transceiver array coil. Magn Reson Med 2005;54(6):1503-1518.

3. Vaughan JT, Snyder CJ, DelaBarre LJ, Bolan PJ, Tian J, Bolinger L, Adriany G, Andersen P, Strupp J, Ugurbil K. Whole-body imaging at 7T: preliminary results. Magn Reson Med 2009;61(1):244-248.

4. Collins CM, Liu W, Swift BJ, Smith MB. Combination of optimized transmit arrays and some receive array reconstruction methods can yield homogeneous images at very high frequencies. Magn Reson Med 2005;54(6):1327-1332.

5. Mao W, Smith MB, Collins CM. Exploring the limits of RF shimming for high-field MRI of the human head. Magn Reson Med 2006;56(4):918-922.

6. Katscher U, Bornert P, Leussler C, van den Brink JS. Transmit SENSE. Magn Reson Med 2003;49(1):144-150.

7. Metzger GJ, Snyder C, Akgun C, Vaughan T, Ugurbil K, Van de Moortele PF. Local B1+ shimming for prostate imaging with transceiver arrays at 7T based on subject-dependent transmit phase measurements. Magn Reson Med 2008;59(2):396-409.

8. Grissom W, Yip CY, Zhang Z, Stenger VA, Fessler JA, Noll DC. Spatial domain method for the design of RF pulses in multicoil parallel excitation. Magn Reson Med 2006;56(3):620-629.

9. Orzada S, Maderwald S, Poser BA, Bitz AK, Quick HH, Ladd ME. RF excitation using time interleaved acquisition of modes (TIAMO) to address

B1 inhomogeneity in high-field MRI. Magn Reson Med 2010;64(2):327-333.

10. Griswold MA, Jakob PM, Heidemann RM, Nittka M, Jellus V, Wang J, Kiefer B, Haase A. Generalized autocalibrating partially parallel acquisitions (GRAPPA). Magn Reson Med 2002;47(6):1202-1210.

11. Christ A, Kainz W, Hahn EG, Honegger K, Zefferer M, Neufeld E, Rascher W, Janka R, Bautz W, Chen J, Kiefer B, Schmitt P, Hollenbach HP, Shen J, Oberle M, Szczerba D, Kam A, Guag JW, Kuster N. The Virtual Family--development of surface-based anatomical models of two adults and two children for dosimetric simulations. Physics in medicine and biology 2010;55(2):N23-38.

12. Ackerman MJ, Spitzer VM, Scherzinger AL, Whitlock DG. The Visible Human data set: An image resource for anatomical visualization. Medinfo 1995;8:1195-1198.

13. Orzada S, Kraff O, Schäfer LC, Brote I, Bahr A, Bolz T, Maderwald S, Ladd ME, Bitz AK. 8-channel transmit/receive head coil for 7 T human imaging using intrinsically decoupled strip line elements with meanders. In: Proceedings of the 17th Annual Meeting of ISMRM, Honolulu, HI, USA 2009; (Abstract 3010).

14. Orzada S, Quick HH, Ladd ME, Bahr A, Bolz T, Yazdanbakhsh P, Solbach K, Bitz AK. A flexible 8-channel transmit/receive body coil for 7 T human imaging. In: Proceedings of the 17th Annual Meeting of ISMRM, Honolulu, HI, USA 2009; (Abstract 2999).

15. Lagarias JC, Reeds JA, Wright MH, Wright PE. Convergence properties of the Nelder-Mead Simplex Method in low dimensions. SIAM Journal of Optimization 1998;9(1):112-147.

16. Bitz AK, Brote I, Orzada S, Kraff O, Maderwald S, Quick HH, Yazdanbakhsh P, Solbach K, Bahr A, Bolz T, Wicklow K, Schmitt F, Ladd ME. An 8-channel

add-on RF shimming system for whole-body 7 Tesla MRI including real-time SAR monitoring. presented at the 17th Annual Meeting of ISMRM, Honolulu, HI, USA, April 18-24 2009.

17. Yazdanbakhsh P, Held S, Brote I, Bitz AK, Orzada S, Ladd ME, Solbach K. 16-Bit Vector Modulator for B1 Shimming in 7T MRI. In: Proceedings of the 17th Annual Meeting of ISMRM, Honolulu, HI, USA 2009; (Abstract 4768).

18. Butler J, Lowe R. Beam forming matrix simplifies design of electronically scanned antennas. Electron Design 1961;9:170.

19. Katscher U, Vernickel P, Nehrke K, Graeslin I. Improving RF Shimming Via Non-Linear Sub-Image Combination. In: Proceedings of the 18th Annual Meeting of ISMRM, Stockholm, Sweden 2010;(Abstract 4919).

20. Haacke EM, Brown RW, Thompson MR, Venkatesan R. Magnetic Resonance Imaging: Physical Principles and Sequence Design. NY: John Wiley & Sons; 1999. 454-455 p.

Chapter 5 Mitigation of B_1^+ Inhomogeneity on Single-Channel Transmit Systems with TIAMO*

Abstract

In magnetic resonance imaging (MRI) there has been a constant drive to higher static magnetic field strengths (B_0) to achieve a higher signal-to-noise ratio and new or enhanced contrasts. In today's high-field systems, severe problems regarding the homogeneity of the transmission field are encountered.

Recently, an acquisition scheme called Time-Interleaved Acquisition of Modes (TIAMO) has been proposed to tackle the inhomogeneity problems in high-field MRI. The basic premise is to excite two (or more) different B_1^+ modes using static RF shimming in an interleaved acquisition, where the complementary RF patterns of the two modes can be exploited to improve overall signal homogeneity. In its usual implementation, a multi-channel transmit system is required.

In this work the goal is to present a simple and inexpensive hardware setup which makes it possible to use TIAMO on any single-channel transmit system while making use of the vendor-provided single-channel RF safety system. To demonstrate the efficacy of this setup, spin echo images from the pelvis are acquired at 7 Tesla exhibiting no complete signal dropouts.

***Orzada S**, Maderwald S, Johst S, Bitz AK, Solbach K, Ladd ME.
"Mitigation of B1+ Inhomogeneity on Single-Channel Transmit Systems with TIAMO"
Magn Reson Med. 2012, [in press]

5.1 Introduction

In magnetic resonance imaging (MRI) there has been a constant drive to higher static magnetic field strengths (B_0) to achieve a higher signal-to-noise ratio and new or enhanced contrasts. In today's high-field systems, severe problems regarding the homogeneity of the transmission field are encountered (1,2). Since the operational frequency is proportional to B_0, the wavelength approaches the size of the human head/body. This results in wave effects which lead to signal decreases and dropouts, making especially whole-body imaging challenging (3).

Several methods have been proposed to tackle these problems. Most of these methods are multichannel methods. Of these, the two most noted are RF shimming (4,5) and Transmit SENSE (6). While standard clinical systems at lower field strengths are normally equipped with only a single-channel transmit (Tx) system, multichannel Tx solutions have been introduced for high-field systems but necessitate additional expensive hardware. A complete RF chain including modulation of the operational frequency, power amplification, and SAR supervision has to be provided for each transmit channel (7-9).

Recently, an acquisition scheme termed Time-Interleaved Acquisition of Modes (TIAMO) has been proposed to tackle Tx field inhomogeneity problems (10,11). The basic premise is to excite two (or more) different B_1^+ modes using static RF shimming in an interleaved acquisition, where the complementary RF patterns of the two modes can be exploited to improve overall signal homogeneity. The cost in time for acquiring multiple images can at least partly be compensated by using the multiple transmit modes to form virtual receive elements to improve GRAPPA (12) reconstruction performance, thereby making higher parallel imaging acceleration factors feasible in conjunction with TIAMO. It can be shown that although the RF pattern of each transmit setting used for acquisition is in itself inhomogeneous, correct image contrast can be achieved (11). First sets of nearly homogeneous 7 Tesla images from throughout the body were shown in (10) and (13).

In this work the goal is to present a simple and inexpensive hardware setup which makes it possible to use TIAMO on any single-channel Tx system while making use of the vendor-provided single-channel RF safety system.

5.2 Materials and Methods

A schematic overview of the hardware setup for TIAMO on a single channel Tx system is given in Figure 5.1. It consists of a high-power switch connected to two inputs (360° phase cycle (CP^{+}) and 720° phase cycle (CP^{2+})) of a planar Butler matrix (14,15) of 2^n x 2^n channels, where n is a positive integer. The outputs of this Butler matrix are connected to a Tx or Tx/Rx coil with 2^n channels. The switch is toggled via the controller box by an impulse sent by the scanner after each echo or echo train. The input of the switch is connected to the scanner's supervised high-power RF output.

In this study an 8-channel Tx/Rx coil was used with a planar Butler Matrix of 8 x 8 channels.

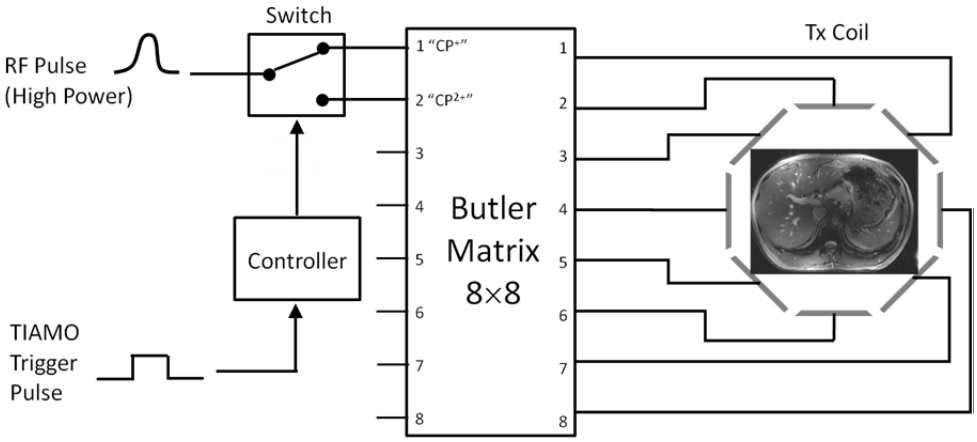

Figure 5.1: *Schematic overview of the hardware setup proposed for TIAMO on single-channel systems, here for the example of an 8 x 8 Butler matrix and an 8-channel transmit coil.*

High-power RF switch

The electrical schematic of the high-power RF switch is given in Figure 5.2A. It consists of two pairs of PIN diodes and two transmission lines of a quarter wavelength each, as well as blocking circuitry to block both DC from the RF path and RF from the DC bias path. If a voltage is applied, one of the pairs of diodes is conducting forming a short for RF, while the other pair is not conducting forming an open for RF. The short is transformed to an open at the RF feeding point by the quarter wavelength transmission line.

The capacitor C_{short} accounts for the effective inductance of the PIN diodes and is used as a DC block. Its value was determined experimentally to maximize the isolation in the off-state. Since the peak voltage and current at this capacitor can be very large, the capacitor is a Voltronics 25 Series capacitor with a working voltage of 2500 V.

The resistors R_1 and R_2 are used to limit the DC current through each diode to 100 mA. The LC tank circuits are tuned to 300 MHz to block RF from the DC path. C_{harm} is used to form a low-pass filter to block any harmonics above the frequency range of the LC tanks. The switch is mounted inside a small box measuring 11 x 11 x 6 cm^3.

Controller circuitry

The electrical schematic of the RF switch controller is given in Figure 5.2B. It consists of four major stages, supplied by an independent power supply ($\pm U_c = \pm 10$ V DC) not shown in the schematic. The first stage is the trigger signal stage, with a toggle switch driven either by an external trigger or a manual trigger from the impulse push button. The starting state of the controller is of no importance in TIAMO since the chronological order of the two modes does not have any influence on the reconstruction or the resulting image. The manual

trigger was implemented for compatibility with sequences not using TIAMO, so that the desired mode could be manually selected.

The second stage consists of a D flip-flop, where the negative output is fed back to the input to make it a toggle flip-flop. A network is used to reduce the supply voltage $\pm U_c$ to ±2.6 V, since the flip-flop's architecture allows an absolute maximum supply voltage of 7 V and the maximum recommended supply voltage is 6 V. The third stage is a pre-amplification stage that transforms the ±2.6 V output voltage of the flip-flop to $\pm U_c$, the supply voltage of the controller. The fourth stage is the power stage consisting of two MOSFETs that have a resistance of less than 0.1 Ω in the on-state.

A band-stop filter (not shown in the schematic) with an attenuation of -70 dB at the center frequency of 300 MHz is connected to the output of the controller to prevent RF close to the operating frequency of the scanner being sent into the scanner room. The controller setup including filter, power supply, and fuses fits into a box measuring 16 x 13 x 8 cm^3.

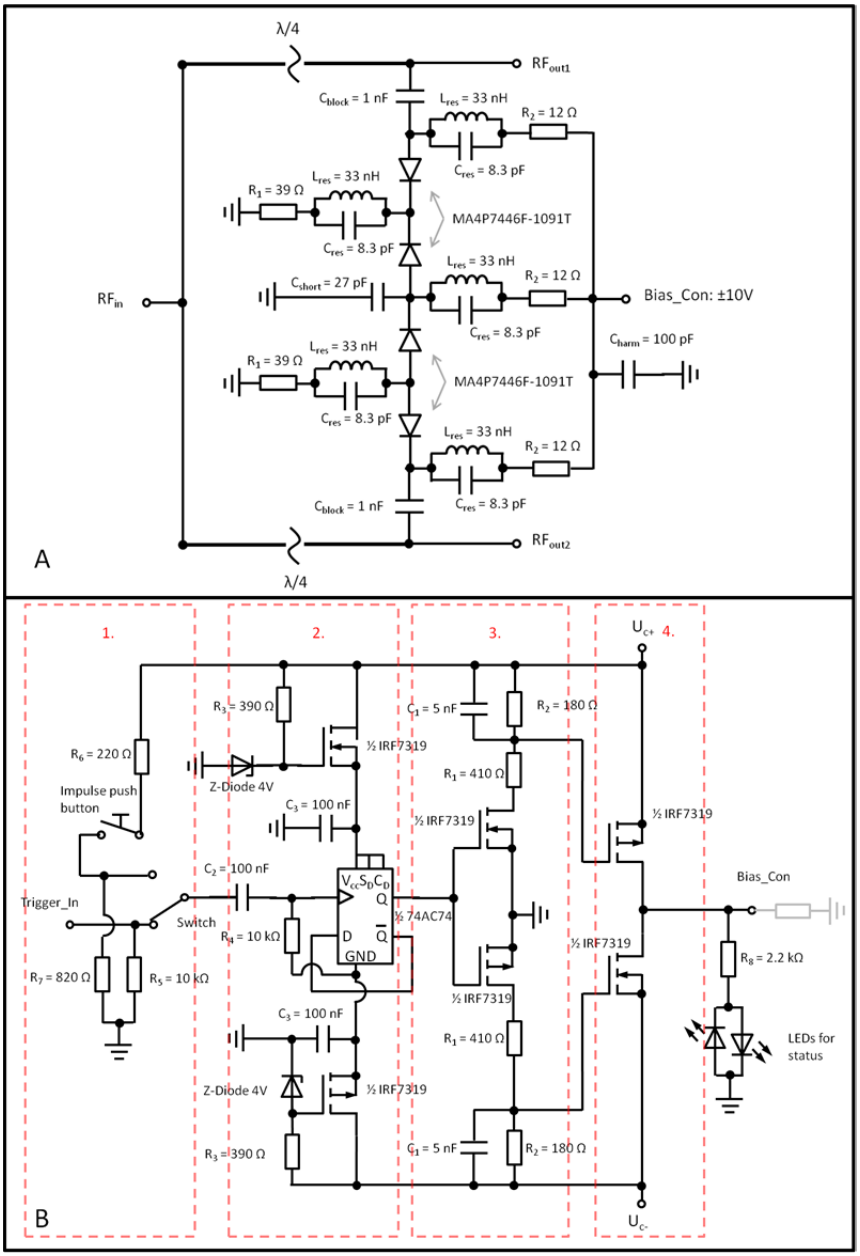

Figure 5.2: A) Electrical schematic of the high-power RF switch with PIN diodes. B) Electrical schematic of the switch controller; the four stages indicated by the dashed rectangles are described in the text.

Imaging setup

All imaging experiments were conducted on a Siemens 7T whole-body system (Magnetom 7T, Siemens Healthcare, Erlangen, Germany) using gradients with maximum amplitude of 40 mT/m and maximum slew rate of 200 mT/m/ms. The software version was VB17. For RF transmission, the vendor-provided power amplifier was utilized (LPPA 13080W, Dressler HF Technik GmbH, Stolberg, Germany).

An in vivo imaging experiment was performed in a male volunteer (80 kg, 1.86 m) using an eight-channel flexible body array with meanders (16). The array fits closely to the body and is driven with an 8x8-channel planar Butler matrix (15) that has an overall insertion loss of 0.73 dB.

The maximum permissible input power for the coil and the subject's position was determined by full-wave simulations and post processing. The simulations were performed in CST Microwave Studio (CST AG, Darmstadt, Germany) in three different body models (HUGO (17), DUKE and ELLA (18)). The post processing was performed in Matlab (The Mathworks, Natick, MA, USA). To get the maximum permissible input power, the voxel-based SAR of the TIAMO acquisition was estimated by averaging the voxel-based SAR of the two utilized RF modes to account for the interleaved excitation (11). This is possible because the two modes are not transmitted simultaneously, but in quick succession, so therefore their E-fields don't interact directly and their contribution to tissue heating is additive. Afterwards, the SAR 10g-average of the modes was evaluated from these averaged voxel values, from which the maximum permissible input power could be derived. This power value was supplied to the vendor-provided single-channel SAR supervision system.

A 2D Turbo Spin Echo (TSE) sequence was used with a TR of 3000 ms, a TE of 46 ms, an echo train length of 7, a bandwidth of 698 Hz per pixel, an image acquisition matrix of 384 x 512, a field-of-view of 262 x 350 mm², and a slice thickness of 4 mm, resulting in a non-interpolated resolution of 0.68 x 0.68 x 4 mm³. The sequence was slightly modified to provide an additional

trigger pulse after each echo train to toggle the RF power switch. Images were acquired with the CP^+ mode and the CP^{2+} mode individually, and with a TIAMO acquisition utilizing both of these RF modes. The CP^+ and CP^{2+} modes were chosen for the TIAMO acquisition because previous work has shown that they come close in performance to modes optimized for B_1^+ homogeneity in an axial slice in the middle of the coil (11) and because they are easy to realize with a Butler matrix.

The conventional acquisitions (CP^+ and CP^{2+}) were accelerated with GRAPPA in conjunction with an acceleration factor of $R = 2$ using the 8 "real" receive elements, while the TIAMO image was accelerated by a factor of $R = 4$ using the 16 "virtual" receive elements for reconstruction. In all cases, 24 reference lines were used; therefore, the acquisition time for the TIAMO image (TA = 99 s) was 13.8% greater than that of each individual mode (TA = 87 s). Reconstruction of the images was performed by the vendor-provided image calculation system. A marginal modification to the vendor-provided reconstruction software was used that reorders the raw data of two interleaved acquisitions before the standard reconstruction such that these data are treated as one acquisition with twice the number of receive elements. No intensity correction was used in the reconstruction. The switch and the controller circuitry were in place during the whole experiment. For the conventional acquisition, the controller was set to manual triggering so that the transmit mode could be selected.

5.3 Results

The switching time of the controller and the RF switch is approximately 10 µs. In the off-state of an output channel, the attenuation of the signal is -30.5 dB, and in the on-state it is 0.45 dB. The switch was tested to withstand a 1 ms pulse of the full RF peak power that the scanner's amplifiers can deliver at the patient table (ca. 6 kW) and a continuous average power of at least 80 W. The amplitude levels of the harmonics were measured to be at least 50 dB lower than the amplitude at the working frequency, and these levels were not enhanced by the power switch, indicating that no significant clipping occurred due to charge starvation. Isolation and insertion loss at the peak power only increased by 0.2 dB compared to low power. Power loss in the controller during switching is low, so that the controller can manage at least 10,000 switching cycles per second.

Figure 5.3 shows TSE images from the pelvis of a human volunteer. To stay within the 10 W/kg SAR_{10g} limit, the total maximum permissible input powers at the input ports of the coil for CP^{+}, CP^{2+}, and TIAMO were 58W, 45W, and 55W, respectively. Images 5.3A and 5.3B show the CP^{+} and CP^{2+} modes of the coil acquired individually. Apparent signal dropouts of the Tx modes are marked in the images. The TIAMO image 5.3C exhibits no complete signal dropout over the entire axial slice. Images 5.3D and 5.3E show the normalized signal intensity of the CP^{+} and CP^{2+} images relative to the TIAMO image to further illustrate the position of signal dropouts. Measurements with the method described in (19) show that the mean SNR of the TIAMO image is approximately 75% of the SNR of each acquisition with a single mode, but the SNR distribution is more homogenous and in particular there are no regions with zero SNR as can be found in the single-mode images.

The set of images in Figure 5.3F shows 11 simultaneously acquired axial TIAMO TSE images covering 12 cm in the head-feet direction, all without any complete signal dropouts.

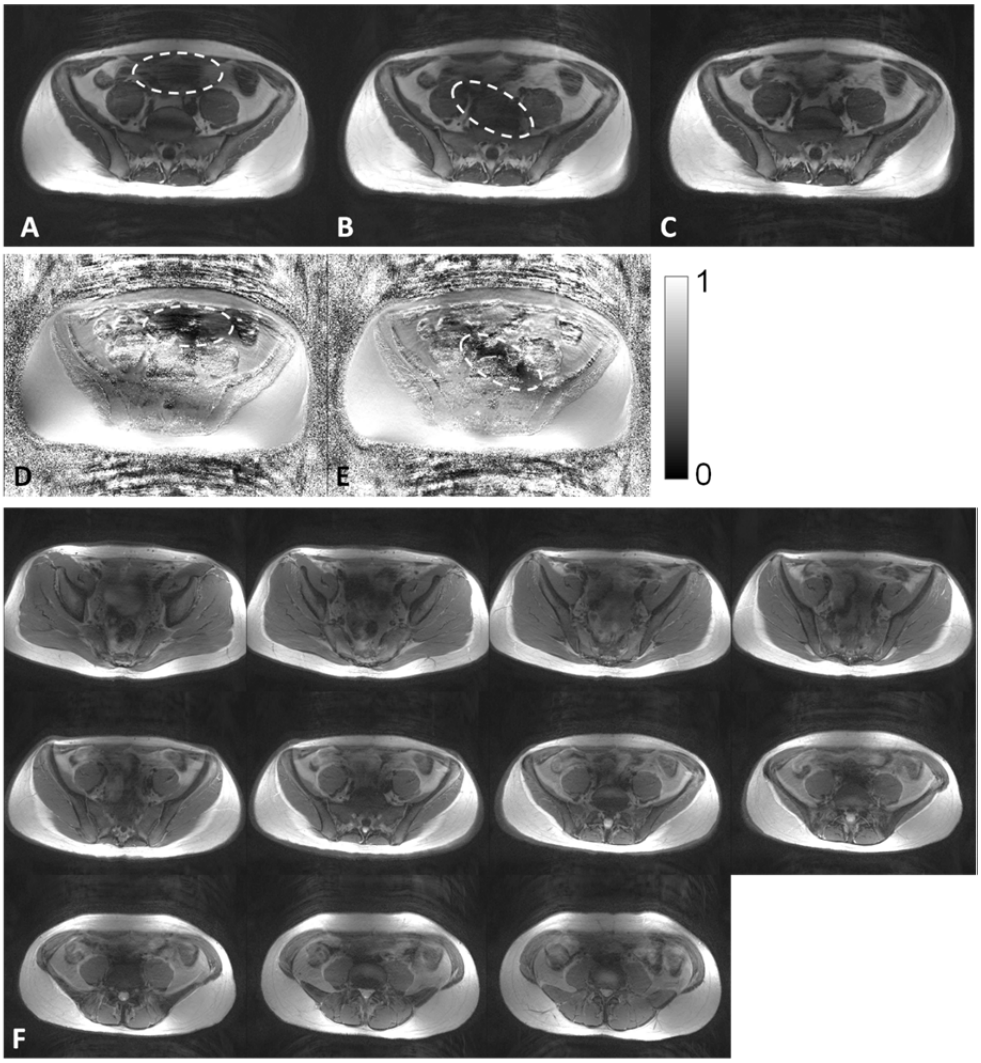

Figure 5.3: *Pelvic T2-weighted TSE images of a human volunteer with a non-interpolated resolution of 0.68 x 0.68 x 4 mm³ acquired with A) the CP^{+} mode and B) the CP^{2+} mode (both GRAPPA R = 2). The differing location of the most significant signal dropout, where the signal and therefore the SNR drop to 0, is marked. C) TIAMO reconstructed image with the interleaved acquisition of the CP^{+} and CP^{2+} modes took only 14% more acquisition time (GRAPPA R = 4) than an individual mode; no complete signal dropout is visible. D) and E) show the signal*

intensity of the CP^{+} and CP^{2+} images normalized to the TIAMO image in arbitrary units to illustrate the position of the dropouts. F) shows a set of 11 TIAMO images from the male pelvis covering 12 cm in the head-feet direction, showing no complete signal dropouts and therefore no regions where the SNR drops to 0.

5.4 Discussion

These experiments demonstrate that significantly improved B_1^+ homogeneity can be achieved at 7T with a simple hardware setup without a complicated multichannel Tx system. The hardware for the controller and the RF switch costs only about $150 including connectors and housing, while the hardware for the Butler matrix costs about $1500, and most of the RF chain of a single-channel Tx system can be utilized including the conventional SAR supervision. In principle, any two-port coil could be used if the two ports produce more or less complementary B_1^+ distributions with dropouts in distinct locations.

The switching time of 10 µs is more than sufficient for TIAMO. In previous experiments (10,11) the switching time of the modulators used was 540 µs, which was still sufficient because switching to the next RF mode can be performed during data sampling under the read-out gradient. The new switch is more than a factor of 50 faster. The switch can withstand enough RF power and switching frequency for any conventional imaging sequence that can be run on the scanner, and the tested switching cycle should be more than sufficient for any sequence using TIAMO.

The presented electronics were designed to be compatible with the specific MR system utilized here. Implementations for other systems should of course take into consideration the specifics of the particular MR system to ensure proper operation and protection of the hardware.

In the TSE imaging example presented here, it could be shown in practice that by using a higher acceleration factor, the time penalty for acquiring two images could be reduced from a factor of 2 to a factor of about 1.14 with only a small loss in mean SNR. This was done by taking advantage of the virtual elements in the TIAMO acquisition, which enable higher acceleration factors as previously shown (10). The virtual elements are of course not able to reduce the g-factor to 1. Although the g-factor for the TIAMO images is slightly higher overall for R = 4 versus the R = 2 of the individual modes, the minimum SNR is still higher than in

the individual images, where it is zero in the regions of the complete signal dropouts.

Additionally, the imaging experiments show that this simple setup is capable of delivering T2-weighted TSE images of the male pelvis which are free of complete signal dropouts. This is consistent with earlier work (13) which showed that TIAMO using a combination of the CP^{+} and CP^{2+} modes can deliver images without complete signal dropouts throughout the whole body.

5.5 Conclusion

In this work we presented an inexpensive, easy-to-use, and robust hardware configuration that is capable of performing TIAMO imaging on an MRI system with a single transmit channel under the control of the vendor-provided SAR supervision system. It could be shown that spin echo imaging at 7T without complete signal dropouts is feasible in the human pelvis with this setup. Previous results with the same TIAMO technique, but with a more complicated hardware setup, have shown that imaging without complete signal dropouts is feasible throughout the body.

References

1. Hoult DI, Phil D. Sensitivity and power deposition in a high-field imaging experiment. J Magn Reson Imaging 2000;12(1):46-67.

2. Van de Moortele PF, Akgun C, Adriany G, Moeller S, Ritter J, Collins CM, Smith MB, Vaughan JT, Ugurbil K. B(1) destructive interferences and spatial phase patterns at 7 T with a head transceiver array coil. Magn Reson Med 2005;54(6):1503-1518.

3. Vaughan JT, Snyder CJ, DelaBarre LJ, Bolan PJ, Tian J, Bolinger L, Adriany G, Andersen P, Strupp J, Ugurbil K. Whole-body imaging at 7T: preliminary results. Magn Reson Med 2009;61(1):244-248.

4. Collins CM, Liu W, Swift BJ, Smith MB. Combination of optimized transmit arrays and some receive array reconstruction methods can yield homogeneous images at very high frequencies. Magn Reson Med 2005;54(6):1327-1332.

5. Mao W, Smith MB, Collins CM. Exploring the limits of RF shimming for high-field MRI of the human head. Magn Reson Med 2006;56(4):918-922.

6. Katscher U, Bornert P, Leussler C, van den Brink JS. Transmit SENSE. Magn Reson Med 2003;49(1):144-150.

7. Setsompop K, Wald LL, Alagappan V, Gagoski B, Hebrank F, Fontius U, Schmitt F, Adalsteinsson E. Parallel RF transmission with eight channels at 3 Tesla. Magn Reson Med 2006;56(5):1163-1171.

8. Graeslin I, Biederer S, Falaggis K, Vernickel P, Dingemans H, Mens G, Roeschmann P, Leussler C, Zhai Z, Morich M, Katscher U. Realtime SAR monitoring to ensure patient safety for parallel transmission systems. In: Proceedings of the 15th Annual Meeting of the ISMRM, Berlin, Germany 2007;Abstract 170.

9. Bitz AK, Brote I, Orzada S, Kraff O, Maderwald S, Quick HH, Yazdanbakhsh P, Solbach K, Bahr A, Bolz T, Wicklow K, Schmitt F, Ladd ME. An 8-channel add-on RF shimming system for whole-body 7 Tesla MRI including real-time SAR monitoring. In: Proceedings of the 17th Annual Meeting of ISMRM, Honolulu, HI, USA 2009;Abstract 4767.

10. Orzada S, Maderwald S, Poser BA, Bitz AK, Quick HH, Ladd ME. RF excitation using time interleaved acquisition of modes (TIAMO) to address B1 inhomogeneity in high-field MRI. Magn Reson Med 2010;64(2):327-333.

11. Orzada S, Maderwald S, Poser BA, Johst S, Kannengiesser S, Ladd ME, Bitz AK. Time Interleaved Acquisition of Modes (TIAMO): an Analysis of SAR and Image Contrast Implications. Magn Reson Med 2011;67(4):1033-1041.

12. Griswold MA, Jakob PM, Heidemann RM, Nittka M, Jellus V, Wang J, Kiefer B, Haase A. Generalized autocalibrating partially parallel acquisitions (GRAPPA). Magn Reson Med 2002;47(6):1202-1210.

13. Orzada S, Maderwald S, Kraff O, Brote I, Ladd ME, Solbach K, Yazdanbakhsh P, Bahr A, Fautz H-P, Bitz AK. 16-channel Tx/Rx body coil for RF shimming with selected Cp modes at 7T. In: Proceedings of the 17th Annual Meeting of ISMRM, Honolulu, HI, USA 2010; Abstract 50.

14. Butler J, Lowe R. Beam forming matrix simplifies design of electronically scanned antennas. Electron Design 1961;9:170.

15. Yazdanbakhsh P, Solbach K. Microstrip Butler matrix design and realization for 7 T MRI. Magn Reson Med;66(1):270-280.

16. Orzada S, Quick HH, Ladd ME, Bahr A, Bolz T, Yazdanbakhsh P, Solbach K, Bitz AK. A flexible 8-channel transmit/receive body coil for 7 T human imaging. In: Proceedings of the 17th Annual Meeting of ISMRM, Honolulu, HI, USA 2009; (Abstract 2999).

17. Ackerman MJ, Spitzer VM, Scherzinger AL, Whitlock DG. The Visible Human data set: An image resource for anatomical visualization. Medinfo 1995;8:1195-1198.

18. Christ A, Kainz W, Hahn EG, Honegger K, Zefferer M, Neufeld E, Rascher W, Janka R, Bautz W, Chen J, Kiefer B, Schmitt P, Hollenbach HP, Shen J, Oberle M, Szczerba D, Kam A, Guag JW, Kuster N. The Virtual Family--development of surface-based anatomical models of two adults and two children for dosimetric simulations. Physics in medicine and biology 2010;55(2):N23-38.

19. Kellman P, McVeigh ER. Image reconstruction in SNR units: a general method for SNR measurement. Magn Reson Med 2005;54(6):1439-1447.

Chapter 6 Summary

Even though 7 Tesla systems have been available for more than 10 years, they are still not integrated into clinical routine and are currently only used as pure research systems. In head imaging, where the technical challenges are much more modest compared to whole-body imaging, much clinical research is being performed, and it appears that 7 Tesla head imaging may be going clinical soon. Body imaging is still challenging and will surely take more development time. The key challenges are the presence of strong inhomogeneities in the transmit field and limitations due to SAR. From these arise strong need for specially developed multichannel transmit coils as well as for methods to transmit with these coils. These methods need to be safe, robust, and easy to use.

In this thesis the concept for a novel transmit array for imaging of the ankle at 7 Tesla is presented that is capable of applying new transmit strategies with eight transmit channels. This array can be used for real-time imaging of the moving ankle joint as well as high resolution imaging. It has been thoroughly tested and evaluated in terms of SNR, g-factor, and patient safety.

Since coil design alone is not enough to cope with the special needs of 7 Tesla body imaging, the TIAMO method was developed which is capable of producing fairly homogeneous images with minimal effort. The theory of the virtual elements in TIAMO was formulated as well as the theory for the contrast in spoiled gradient echo TIAMO. MRI experiments were conducted to explore TIAMO's impact on the g-factor and on contrast in many different sequences and contrast types. Also, numerical experiments were conducted to show TIAMO's impact on homogeneity and SAR. Finally, a hardware setup was developed that enables the use of TIAMO on single-channel transmit systems with only a single channel of SAR supervision.

TIAMO has proven to be an easy to use and robust method for coping with the severe signal dropouts in 7 Tesla whole-body imaging. It is superior to RF shimming in terms of homogeneity, while at the same time its efficiency in terms

of SAR is better. In abdominal imaging with an eight-channel coil, one can ameliorate the signal dropouts that are always present with simple RF shimming. It is clear that Transmit SENSE is superior in the degrees of freedom it offers when trying to homogenize the excitation. On the other hand, TIAMO is much easier to implement and very robust. As was demonstrated, even a single-channel transmit system can be equipped for use of TIAMO with the addition of only a few low-cost components. This makes TIAMO an interesting alternative to other methods of coping with the homogeneity problems of the transmit field, especially since at the moment it is much closer to being clinically applicable than the more sophisticated Transmit SENSE approach.

In conclusion, this work presents new methods for 7 Tesla imaging outside of the brain that can not only widely expand the options for clinical research but also have the potential to move 7 Tesla closer to clinical application.

Chapter 7 Samenvatting

Hoewel 7T systemen al meer dan 10 jaar beschikbaar zijn, zijn ze nog altijd niet geïntegreerd in de klinische praktijk en worden ze uitsluitend als onderzoekssystemen gebruikt. Er wordt veel onderzoek gedaan naar afbeelding van het hoofd, waarbij de technische uitdagingen veel bescheidener zijn dan in afbeelding van het hele lichaam, en het lijkt erop dat afbeelding van het hoofd op 7T binnenkort in de kliniek geïntroduceerd kan worden. Afbeelding van het lichaam blijft een grotere uitdaging, en zal zonder twijfel meer ontwikkelingstijd kosten. De grootste uitdagingen zijn de sterke inhomogeniteiten in het zendveld en SAR-limitaties. Om hieraan het hoofd te bieden moeten zowel speciaal ontworpen meerkanaals zendspoelen als methoden om met deze spoelen te zenden worden ontworpen. Deze methoden moeten veilig, robuust en gemakkelijk in het gebruik zijn.

In dit proefschrift wordt een nieuw concept voor een meerkanaals zendspoel voor het afbeelden van de enkel op 7 Tesla gepresenteerd, waarmee het mogelijk is nieuwe zendmethoden met acht kanalen toe te passen. Deze spoel kan zowel worden gebruikt voor real-time afbeelding van het bewegende enkelgewricht als voor hoge-resolutie afbeelding. Tests en evaluaties van deze spoel in termen van SNR, g-factor en patiëntveiligheid worden uitgebreid behandeld.

Omdat spoelontwerp alleen niet genoeg is om met de speciale benodigdheden van afbeelding van het lichaam op 7T om te gaan is de TIAMO-methode ontwikkeld, die het produceren van redelijk homogene beelden sterk vergemakkelijkt. Een formulering voor de theorie van virtuele spoelelementen in TIAMO, en een formulering voor het contrast in spoiled gradient echo TIAMO zijn opgesteld. MRI experimenten zijn uitgevoerd om het effect van TIAMO op de g-factor en het contrast in verscheidene sequenties en contrasttypen te onderzoeken. Daarnaast zijn numerieke experimenten uitgevoerd om het effect van TIAMO op homogeniteit en SAR te onderzoeken. Tot slot is een hardware-opstelling ontwikkeld die het mogelijk maakt om TIAMO te gebruiken op een éénkanaals zendsysteem, waarbij ook éénkanaals SAR-supervisie toereikend is.

Het is gebleken dat TIAMO een robuuste en gebruiksvriendelijke methode is om het sterke locale signaalverlies in 7 Tesla afbeelding van het lichaam tegen te gaan. Het is beter dan RF shimming in termen van homogeniteit, en heeft tegelijkertijd een betere SAR-efficiëntie. Locale gebieden van signaalverlies kunnen in abdominale afbeelding met een achtkanaalsspoel met eenvoudige RF-shimming worden verminderd. Transmit SENSE is duidelijk superieur aan TIAMO voor het homogeniseren van excitatie, vanwege het grotere aantal vrijheidsgraden dat deze techniek biedt. TIAMO is echter veel gemakkelijker te implementeren en zeer robuust. Ook kan zelfs een éénkanaals zendsysteem worden uitgerust voor gebruik met TIAMO, met toevoeging van slechts een paar goedkope componenten. Dit maakt TIAMO tot een interessant alternatief om de homogeniteitsproblemen van het zendveld aan te pakken, vooral omdat het momenteel veel dichterbij klinische toepasbaarheid is dan het veel complexere Transmit SENSE.

In dit werk worden nieuwe methoden voor afbeelding buiten het brein bij 7 Tesla gepresenteerd, die niet alleen de mogelijkheden voor klinisch onderzoek sterk verruimen, maar die ook de potentie hebben om 7 Tesla afbeelding dichter bij toepassing in de kliniek te brengen.

Acknowledgement

This work was contributed to by many people in many different ways and would not have been possible without their valued contributions.

First of all I would like to thank Mark Ladd for giving me the opportunity to work at the Erwin L. Hahn Institute. Thank you for your continued support and the excellent working conditions I found at the Institute and for giving me the freedom to follow any (sometimes weird) ideas I had for investigations. I very much enjoyed the spirit in the workgroup and I am proud to have had the opportunity to be part of the Hahn Institute becoming one of the leading institutions for 7 Tesla body imaging.

I would like to thank Andreas Bitz for his sharing his expanded knowledge in electrical engineering, for his humor and for not bearing a grudge against me concerning our sometimes heated arguments. Thank you for spending so many hours with the numerical simulation and for your guidance during my work, for pushing me further and generally being a supporting pillar of our group.

Stefan Maderwald, I thank you for sharing your vast knowledge of imaging and application of sequences as well as your exactness when it comes to formulating. Not least I wish to thank you for keeping the Institute from falling apart.

I would also like to thank Sören Johst, Benedikt Poser and Oliver Kraff for their help with sequences and general support as well as their good spirit and fun conversations.

In order of appearance I would like to thank Stefan Kruszona, Mark Oehmigen, Linda Kopp and Maike Lindemann for their work as student assistants who have spent quite some time doing oftentimes cumbersome work for me.

Special thanks go to Sigrid Radermacher, Simone Brunn and Beate Fraß for their constant efforts in keeping the Institute organized. Thank you for always ordering the materials I needed to work at highest priority.

Ivonne Braun receives my thanks for always volunteering when I needed someone to test coils and methods on. You are probably the most skilled volunteer in the world and surely are the most imaged.

I would like to thank Andre Rennings for suggesting to work on my diploma thesis in the field of MRI. In the end this has brought me to the ELH.

I would also like to thank all the clinical and psychological staff from the University Hospital Essen and the University of Duisburg-Essen as well as the people from the Donders Centre and the Radiology of the University Hospital in Nijmegen who I had the opportunity to work with. Thank you for the interesting insights into topics far off from engineering. Special thanks to Marnix Maas for helping with the translation.

More thanks go to my family. Danke Mama und Papa, dass Ihr mich immer unterstützt habt. Abgesehen davon, dass Ihr immer die besten Eltern wart, die man sich wünschen kann, wart Ihr mir immer eine große Hilfe in der Schule, im Studium und während der Doktorarbeit. Viele Probleme habe ich allein dadurch lösen können, dass ich Euch genau erklärt habe, was das Problem ist, auch wenn Ihr wahrscheinlich nicht alles davon verstanden habt.

Opa, danke dass ich mein privates Elektroniklabor auf Deinem Dachboden aufbauen durfte und dass du dich nicht hast aus der Ruhe bringen lassen, wenn es mal nach verbrannter Elektronik gerochen hat oder mehrere Meter Kabel gebrannt haben. Ohne die Vorkenntnisse wären mir viele Dinge sicher nicht so leicht von der Hand gegangen.

Sabrina, Dir danke ich dafür, dass du bist, wie du bist. Ich danke Dir dafür, dass du immer für mich da bist, dass du mir in den Hintern trittst und mich auffängst, dass du mich immer unterstützt und dir meine Ideen anhörst, egal, wie konfus sie sind. Ich bin froh, dass ich Dich habe.

Curriculum Vitae

Stephan Orzada, born July 4th, 1980 in Duisburg, Germany

Education

Since 01/2008	Erwin L. Hahn Institute for MRI / University Hospital Essen, Essen, Germany. PhD Student.
10/2001 – 11/2007	University of Duisburg-Essen, Duisburg, Germany Electrical Engineering with main focus on Communications Technology, Diplomingenieur (Masters degree): 11/2007
08/1990 – 06/2000	Gymnasium in den Filder Benden (High School), Moers, Germany Abitur (high school diploma): 06/2000

Experience

Since 01/2008	Erwin L. Hahn Institute for MRI / University Hospital Essen, Essen, Germany. Research Assistant: RF coils and technology for 7 Tesla MRI
03/2007 – 05/2007	IMST GmbH, Kamp-Lintfort, Germany Internship: Electromagnetic simulations
09/2006 – 11/2006	Siemens Building Technologies, Essen, Germany Internship: Planning of fire-alarm systems
05/2004 – 02/2006	University of Duisburg-Essen, Department of General and Theoretical Electronic Engineering, Duisburg, Germany. Student Research Assistant
02/2002 – 03/2002	Siemens Mobile, Kamp-Lintfort, Germany. Practical: Maintenance of industrial equipment
05/2001 – 06/2001	Siemens KWU, Wesel, Germany. Practical: Basic education in mechanical processing and welding

07/2000 – 04/2001	2.RakArtBtl 150, Wesel, Germany. Military Service

Stipends

2009 – 2011	Educational stipends, International Society for Magnetic Resonance in Medicine (ISMRM), Berkley CA, USA
2011 – 2012	Travel stipends, German Academic Exchange Service

Awards

2012	Magna Cum Laude Merit Award, ISMRM
2011	Gorter Award, 3rd Place, German Chapter ISMRM

Scientific Publications

Original Papers:	5 as first author; 11 as co-author
Conference Abstracts:	16 as first author; >60 as co-author

Patents

Pending:	Time Interleaved Acquisition of Modes (TIAMO) filed October 2010 (Germany Patent Application DE 10 2010 011 968.7)

About the author

Stephan Orzada was born in Duisburg-Hochfeld, Germany the 4th of July, 1980. He grew up with his parents Doris Dorothea Orzada and Rainer Alfred Orzada in Moers, Germany. He completed his secondary education at the Gymnasium in den Filder Benden in 2000 as the best in is age-group. From July 2000 to April 2001 he served in the German army, where he was trained as an artillery scout and received a formal mention for his efforts in training soldiers for their deployment in Kosovo. In the summer semester of 2001 he started studying electrical engineering at the University of Duisburg-Essen, where he obtained his diploma in electrical engineering and information technology with a focus on communication technology. He graduated in 2007 with the thesis “Design of high frequency coils with special consideration of the requirements of Transmit SENSE”. During the work on his diploma thesis at the IMST in Kamp-Lintfort, Germany, he already had the chance to work with the team of the Erwin L. Hahn Institute.

After his graduation, Stephan started working at the Erwin L. Hahn Institute for Magnetic Resonance Imaging, Essen, Germany in 2008 to commence his Ph.D. research in the group of Prof. Dr. sc. techn. Mark E. Ladd. He found a strong interest in many topics of the MR field, including the design of radio frequency coils and electronic circuitry, as well as the development of imaging schemes and programming of various types of programs.

Stephan has received several stipends from the International Society for Magnetic Resonance in Medicine (ISMRM) as well as the German Academic Exchange Service (DAAD). He was awarded the Gorter Award (3rd Place) by the German Chapter of the ISMRM in 2011 and a “Magna Cum Laude” ISMRM merit award in 2012.

Stephan Orzada lives with his fiancé in Mülheim an der Ruhr, Germany. In his free time he enjoys doing sports as well as playing the guitar and piano.

Peer-reviewed publications

Dammann P, Kraff O, Wrede KH, Ozkan N, **Orzada S**, Mueller OM, Sandalcioglu IE, Sure U, Gizewski ER, Ladd ME, Gasser T. Evaluation of hardware-related geometrical distortion in structural MRI at 7 Tesla for image-guided applications in neurosurgery. Academic Radiology;18(7):910-916.

Grams AE, Kraff O, Kalkmann J, **Orzada** S, Maderwald S, Ladd ME, Forsting M, Gizewski ER. Magnetic Resonance Imaging of Cranial Nerves at 7 Tesla. Clin Neuroradiol. 2012 Sep 27. [Epub ahead of print].

Kobus T, Bitz AK, van Uden MJ, Lagemaat MW, Rothgang E, **Orzada S**, Heerschap A, Scheenen TW. In Vivo (31) P MR spectroscopic imaging of the human prostate at 7 T: Safety and feasibility. Magn Reson Med. doi: 10.1002/mrm.24175.

Koopmans PJ, Barth M, **Orzada S**, Norris DG. Multi-echo fMRI of the cortical laminae in humans at 7 T. NeuroImage;56(3):1276-1285.

Kraff O, Bitz AK, Kruszona S, **Orzada S**, Schaefer LC, Theysohn JM, Maderwald S, Ladd ME, Quick HH. An eight-channel phased array RF coil for spine MR imaging at 7 T. Investigative Radiology 2009;44(11):734-740.

Nassenstein K, **Orzada S**, Haering L, Czylwik A, Jensen C, Schlosser T, Bruder O, Ladd ME, Maderwald S. Cardiac magnetic resonance: is phonocardiogram gating reliable in velocity-encoded phase contrast imaging? Eur Radiol. 2012 Mar;22(3):559-68.

Nassenstein K, **Orzada S**, Haering L, Czylwik A, Zenge M, Eberle H, Schlosser T, Bruder O, Muller E, Ladd ME, Maderwald S. Cardiac MRI: evaluation of phonocardiogram-gated cine imaging for the assessment of global und regional left ventricular function in clinical routine. European Radiology;22(3):559-568.

Orzada S, Bitz AK, Schafer LC, Ladd SC, Ladd ME, Maderwald S. Open design eight-channel transmit/receive coil for high-resolution and real-time ankle imaging at 7 T. Medical Physics;38(3):1162-1167.

Orzada S, Maderwald S, Goricke SL, Parohl N, Ladd SC, Ladd ME, Quick HH. Design and comparison of two eight-channel transmit/receive radiofrequency arrays for in vivo rodent imaging on a 7 T human whole-body MRI system. Medical Physics;37(5):2225-2232.

Orzada S, Maderwald S, Johst S, Bitz AK, Solbach K, Ladd ME. Mitigation of B1+ inhomogeneity on single-channel transmit systems with TIAMO. Magn Reson Med 2012; doi: 10.1002/mrm.24453. [Epub ahead of print].

Orzada S, Maderwald S, Poser BA, Bitz AK, Quick HH, Ladd ME. RF excitation using time interleaved acquisition of modes (TIAMO) to address B1 inhomogeneity in high-field MRI. Magn Reson Med;64(2):327-333.

Orzada S, Maderwald S, Poser BA, Johst S, Kannengiesser S, Ladd ME, Bitz AK. Time-interleaved acquisition of modes: an analysis of SAR and image contrast implications. Magn Reson Med;67(4):1033-1041.

Umutlu L, Bitz AK, Maderwald S, **Orzada S**, Kinner S, Kraff O, Brote I, Ladd SC, Schroeder T, Forsting M, Antoch G, Ladd ME, Quick HH, Lauenstein TC. Contrast-enhanced ultra-high-field liver MRI: A feasibility trial. Eur J Radiol. 2011 Aug 20. [Epub ahead of print]

Umutlu L, Kraff O, **Orzada S**, Fischer A, Kinner S, Maderwald S, Antoch G, Quick HH, Forsting M, Ladd ME, Lauenstein TC. Dynamic contrast-enhanced renal MRI at 7 Tesla: preliminary results. Investigative Radiology;46(7):425-433.

Umutlu L, **Orzada S**, Kinner S, Maderwald S, Brote I, Bitz AK, Kraff O, Ladd SC, Antoch G, Ladd ME, Quick HH, Lauenstein TC. Renal imaging at 7 Tesla: preliminary results. European Radiology;21(4):841-849.

Umutlu L, Maderwald S, Kinner S, Kraff O, Bitz AK, **Orzada** S, Johst S, Wrede K, Forsting M, Ladd ME, Lauenstein TC, Quick HH. First-pass contrast enhanced renal MRA at 7 Tesla: initial results. European Radiology; 2012 Oct 14 [Epub ahed of print]